electronics

MDPI

Article

Simulation-Based Ampacity Assessment of Cable Joints Based on Hotspot-Temperature Inversion

Mingxu Chen [1], Xueyan Wang [1], Bingye Zhang [1], Peng Lin [1], Pei Li [2], Yiying Li [2,*] and Guoping Zou [2]

[1] Taizhou Hongchuang Electric Power Group Co., Ltd., Taizhou 318000, China
[2] School of Mechanical and Electrical Engineering, China Jiliang University, Hangzhou 310018, China
* Correspondence: liyiying@cjlu.edu.cn

Abstract

Latent insulation defects complicate the ampacity assessment of high-voltage cable intermediate joints because localized electrical stress may increase without a discernible change in surface temperature. This study develops a simulation-based framework that combines electro-thermal analysis, Gaussian-kernel inversion, and current-limit calculation to investigate the potential incorporation of simulated defect information into allowable-current assessment. A 25-dimensional feature representation supports the estimation of internal hotspot temperature and the numerical discrimination between healthy and defective insulation states. The simulations reveal that micro-scale defects substantially intensify localized electric fields but produce only negligible surface-temperature variations, highlighting the difficulty of assessing internal insulation conditions from thermal measurements alone. Under noise-free simulation conditions, the model demonstrates the numerical separability of healthy and defective insulation states within the simulated dataset. A bisection solver determines the allowable current subject to the hotspot-temperature limit, while an illustrative heuristic derating rule adjusts this current to account for potential risks associated with insulation defects. The framework provides a simulation-based approach for investigating the integration of hotspot-temperature estimation and defect-related current adjustment, while highlighting the need for improved noise robustness and experimental validation before practical application.

Keywords: cable intermediate joint; hotspot-temperature inversion; defect-aware modeling; Gaussian-kernel model; ampacity margin assessment

Check for updates

Academic Editor: Herminio Martínez-García

Received: 1 October 2026
Revised: 30 October 2026
Accepted: 1 November 2026
Published: 5 November 2026

Copyright: © 2026 by the authors. Licensee MDPI, Basel, Switzerland. This article is an open access article distributed under the terms and conditions of the Creative Commons Attribution (CC BY) license.

1. Introduction

High-voltage power cables have been extensively deployed in urban transmission and distribution networks owing to their compact structure and limited land requirements. As one of the most critical cable accessories connecting adjacent cable sections, cable intermediate joints maintain electrical continuity and ensure insulation integrity throughout the cable system. Compared with the cable body, however, cable intermediate joints possess a more complicated multilayer composite structure and are therefore more susceptible to installation defects, localized heat accumulation, and insulation degradation. Consequently, accurate assessment of the internal hotspot temperature and ampacity margin of cable joints is of great significance for improving system reliability and maximizing transmission capacity.

The ampacity of a power cable is fundamentally constrained by the maximum allowable working temperature of its insulation system. In conventional engineering practice,

cable ampacity is determined using standardized thermal models, including steady-state ampacity calculation as well as cyclic and emergency loading methods specified in international standards [1,2]. These analytical approaches provide the theoretical basis for cable design and operation. Nevertheless, the accuracy of these methods is highly dependent on predefined assumptions regarding material properties, installation conditions, thermal resistances, ambient temperature, and heat dissipation boundaries. However, in practical working environments, the thermal conditions of cable joints are continuously affected by dynamic load variations, ventilation conditions, surrounding media, installation configurations, and insulation aging. More critically, the internal hotspot temperature, which directly determines the thermal reliability and ampacity margin of energized cable joints, cannot be measured directly. Therefore, ampacity assessments relying solely on rated ampacity or surface-temperature-based criteria may result in inaccurate estimation of the actual transmission capacity and fail to reliably identify potential overheating risks inside cable joints.

To improve the accuracy of cable thermal analysis, numerous studies have been conducted to refine the boundary conditions and material parameters employed in conventional thermal models. Li et al. investigated the effects of burial depth, soil moisture content, and cable arrangement on the temperature rise and long-term ampacity of directly buried XLPE cables [3]. Liu et al. further quantified the influence of microscopic soil thermal properties on cable thermal resistance, temperature gradients, and allowable ampacity, demonstrating that soil thermal resistance is one of the dominant external factors limiting the current-carrying capability of buried cables [4]. For submarine cable applications, Li et al. proposed a fiber-optic sensing-based temperature inversion method considering burial depth, providing an effective solution for dynamic ampacity assessment where direct temperature measurement is impractical [5].

Since direct measurement of internal conductor temperatures and hotspot temperatures in cable joints remains technically challenging, temperature inversion and ampacity assessment based on measurable operational data have attracted increasing research attention. Surface temperature, ambient temperature, and load current, which are readily accessible through online monitoring systems, can be integrated with physics-based models or machine learning algorithms to reconstruct internal temperature distributions and estimate hotspot temperatures. Zhang et al. established an electromagnetic–thermal coupling model for a 110 kV cable system. They analyzed the relationship between conductor temperature and external surface temperature, providing the theoretical basis for indirect conductor temperature estimation [6]. Tian et al. proposed a non-intrusive hotspot-temperature inversion method for cable joints by combining uniform manifold approximation and projection (UMAP) with an improved sparrow search algorithm (ISSA)-optimized back propagation neural network (BPNN), demonstrating that internal joint temperature can be accurately estimated from external temperature measurements [7]. Subsequently, Zhang et al. proposed a long-term ampacity prediction approach for cable intermediate joints based on radial and axial temperature inversion together with the Prophet forecasting model, in which hotspot-temperature inversion serves as the key step for dynamic ampacity prediction [8]. Zhang et al. further developed a thermal–fluid coupled ampacity assessment framework driven by operational measurements, highlighting the importance of digital models that remain consistent with field monitoring data [9].

Existing hotspot-temperature inversion methods can generally be divided into two categories: physics-based numerical simulation and data-driven intelligent algorithms. In the former category, Liang et al. established an electro-thermal inversion model for 110 kV cable joints and estimated conductor temperature using external temperature gradients [10]. Considerable progress has also been achieved in data-driven approaches.

Song et al. proposed a LassoNet-enhanced back propagation neural network for the real-time hotspot-temperature inversion of power cables [11]. Wu et al. optimized a BP neural network using an improved sparrow search algorithm to estimate conductor temperature indirectly [12]. Gao et al. developed a deep neural network-based intelligent temperature monitoring system for full-field cable temperature prediction [13]. Pang et al. combined microwave radiation sensing with a genetic algorithm (GA)-optimized BP neural network to achieve non-contact internal temperature estimation [14]. In addition, Li et al. established a standardized COMSOL-based simulation framework for the rapid temperature analysis of cables with different voltage levels and insulation structures [15]. These developments have significantly improved hotspot-temperature inversion and ampacity prediction.

Lu et al. investigated the electro-thermal-mechanical coupled field distribution of 110 kV cable joints containing typical interface defects and demonstrated that voids, interfacial gaps, metallic contaminants, and semiconductive impurities significantly distort electric field distribution and increase local temperature rise [16]. Yang et al. established a three-dimensional electro-thermal coupling model for 10 kV XLPE cable joints using COMSOL and quantitatively analyzed the influence of air gaps, moisture droplets, semiconductive protrusions, and copper particles. By combining decision trees, DBO-SVM, and Dempster–Shafer evidence fusion, they further improved defect identification accuracy [17]. Other researchers have investigated the influence of microscopic scratches [18], multiple interface defects [19], copper particle contamination [20], coupled electro-thermal behavior [21], insulation degradation mechanisms [22], baseline electro-thermal field distributions [23], defect-induced electric field enhancement [24,25], crimping defects [26], transient overvoltage conditions [27], insulation degradation assessment [28], and temperature sensor installation [29]. For fault detection and location in underground cables, Tariq et al. proposed an optimized traveling-wave-based solution that improves fault-location accuracy under practical conditions [30]. While traveling-wave methods localize an already-occurred fault, the present study addresses the complementary question of how latent insulation-defect information can be incorporated into an ongoing ampacity margin assessment.

The studies reviewed above establish complementary foundations for internal temperature estimation, ampacity assessment, and defect-induced field analysis. Building on these foundations, the present study focuses on connecting localized insulation-defect information with temperature-based current assessment. Specifically, it examines how a predicted binary insulation state can be used to trigger an additional adjustment to a thermally determined current limit, and how reliably that state can be inferred from simulated surface temperatures. This investigation is motivated by the possibility that localized insulation defects may alter electrical stress while producing only small surface-temperature changes. A temperature-based assessment alone therefore cannot establish dielectric safety, while incorporating defect information requires careful examination of its sensitivity to measurement noise and variations in defect geometry.

The Gaussian process (GP), a Bayesian non-parametric learning algorithm, has demonstrated excellent performance for small-sample learning problems. Gaussian process classification (GPC) has achieved superior classification accuracy over random forests and BP neural networks in small-sample image recognition tasks [31]. Gaussian process regression (GPR) has also been successfully applied to nonlinear traffic flow prediction [32] and the early health-state prediction of lithium-ion batteries through optimized kernel hyperparameters [33]. Nevertheless, existing applications of GP methods mainly concentrate on individual tasks, including regression for continuous temperature estimation or classification for defect identification. In the present study, GPR is used for hotspot-temperature

prediction, whereas defect identification is implemented using a logistically calibrated Gaussian-kernel ridge classifier rather than standard GPC.

To investigate this problem, this paper develops a simulation-based framework that connects hotspot-temperature inversion, binary insulation-defect identification, and defect-informed current adjustment for cable intermediate joints. The contributions are threefold. First, the framework uses a common input representation to estimate hotspot temperature through Gaussian process regression and identify the healthy or defective insulation state through a logistically calibrated Gaussian-kernel ridge classifier. This formulation allows thermal-state estimation and insulation-state identification to be examined under the same simulated operating conditions. Second, the framework separates the thermal current limit, determined by a bisection search using the estimated hotspot temperature, from a subsequent heuristic adjustment activated by the predicted binary defect state. A common derating coefficient is selected from the simulated reference defect cases and applied when a defect is predicted. Third, noise perturbation and strict defect-size and axial-location holdout evaluations are used to assess hotspot-temperature prediction and binary defect identification, thereby examining the limitations of the information supplied to the current-assessment procedure. Compared with the temperature-inversion and ampacity-assessment studies reviewed above, the present framework explicitly introduces a predicted binary insulation state into current-margin assessment. Compared with defect-field analyses, it further examines the use and limitations of this information in a subsequent heuristic current adjustment.

2. Electro-Thermal Coupling Analysis of Cable Intermediate Joints Under Defective Conditions

2.1. Electro-Thermal Coupling Model of the Cable Intermediate Joint

The cross-sectional configuration of the cable intermediate joint is illustrated in Figure 1, while its axial structure is presented in Figure 2. The joint consists of multiple concentric layers, including the conductor, crimping connector, conductive shield, prefabricated insulation body, metallic shielding layer, semiconductive tape, and outer sheath. These components jointly ensure the electrical and thermal performance of the cable joint. The XLPE insulation together with the prefabricated insulation body forms the primary insulation system and withstands the working voltage of the cable. In addition, the stress cone and semiconductive tape are employed to suppress electric field distortion around the insulation cutback and thereby mitigate the risk of partial discharge. The metallic shielding layer equalizes the electric potential along the insulation surface, dissipates induced charges, and shields external electromagnetic interference. The outer sheath provides mechanical protection and isolates the insulation system from moisture, soil, and other environmental influences. A three-dimensional electro-thermal coupling model is established to investigate the thermal behavior of the cable intermediate joint. In the present model, the conductor diameter is 35.0 mm, and the inner semiconducting layer has a radial thickness of 1.0 mm. The XLPE insulation extends from an inner radius of 18.5 mm to an outer radius of 34.4 mm, giving a radial thickness of 15.9 mm. The crimping connector has an inner diameter of 35.0 mm, an outer diameter of 68.8 mm, and an axial length of 94.5 mm. The prefabricated insulation body extends over 616 mm axially, with a maximum outer diameter of 152 mm and a radial thickness of 21.6 mm at the joint center. Its thickness varies along the axial transition sections. The total modeled cable length is 2 m, consisting of both the cable body and the intermediate joint. The soil domain has dimensions of 2 m × 4 m × 3 m. The cable axis is located 1 m below the ground surface, with distances of 2 m from the bottom and lateral boundaries. The geometric dimensions are determined according to the actual

structure of a 110 kV XLPE cable joint, while the material properties of the cable components and joint accessories are summarized in Table 1.

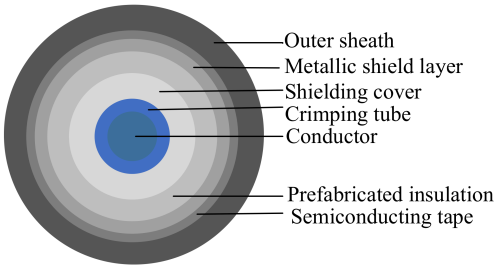

Figure 1. Cross-sectional structure of the 110 kV cable intermediate joint.

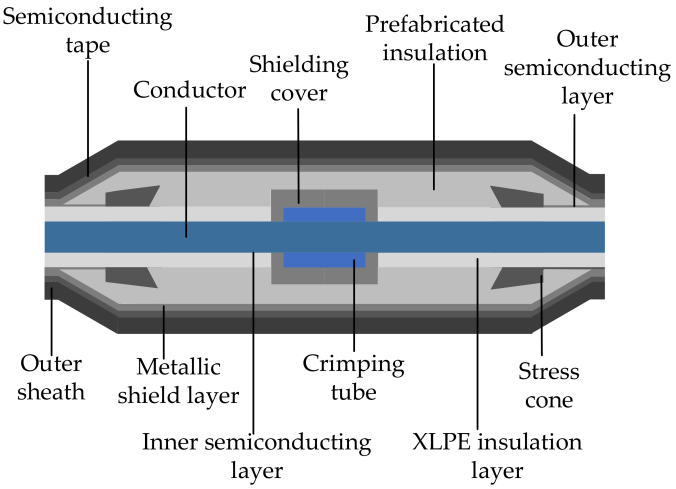

Figure 2. Axial configuration of the three-dimensional cable intermediate joint model.

Table 1. Material properties of the cable body and intermediate joint used in the electro-thermal simulation.

Material	Electrical Conductivity (S/m)	Specific Heat Capacity (J/(kg·K))	Density (kg/m^3)	Thermal Conductivity (W/(m·K))	Relative Permittivity
Copper	5.7×10^7	386	8960	401	1
XLPE	1×10^{-15}	1000	1200	0.29	2.3
Semiconducting	2	1480	1340	0.48	30
Metallic aluminum	3.78×10^7	900	2690	237	1
Silicone rubber	1×10^{-15}	1200	1250	0.35	3.2
Soil	1×10^{-2}	1000	1500	1.5	10

2.2. Electro-Thermal Coupling Simulation

To accurately reproduce the interaction between the electrical and thermal behaviors of the cable intermediate joint during operation, a bidirectional electro-thermal coupling model is established. The coupling strategy adopted in this study is illustrated in Figure 3. The electro-thermal interaction is realized through iterative information exchange between the electrical and thermal fields. During the forward coupling process, the losses caused by the load current are converted into equivalent volumetric heat sources applied to the conductor and crimping connector and are subsequently introduced into the thermal model to calculate the temperature distribution. The calculated temperature field is then fed back to the electrical model during the backward coupling process. Since the electrical

conductivity of metallic conductors varies with temperature, the temperature-dependent electrical conductivity is continuously updated according to the calculated temperature distribution. The updated conductivity is subsequently incorporated into the governing equations of the electric field, resulting in a revised electrical loss distribution. This iterative procedure is repeated until convergence is achieved.

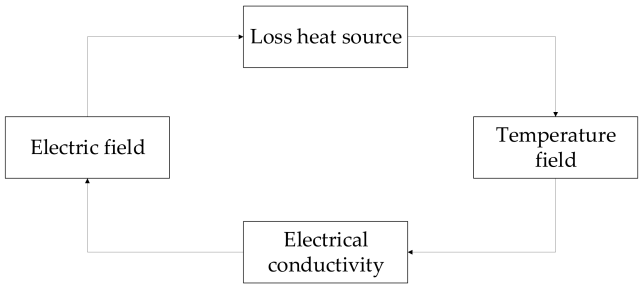

Figure 3. Bidirectional electro-thermal coupling strategy adopted for the cable intermediate joint simulation.

The ground surface is assigned a convective heat-flux boundary with a reference coefficient of 6 W/(m^2·K), and the ambient temperature is varied according to the investigated condition. The bottom soil boundary is maintained at 10 °C, while the remaining outer boundaries are treated as thermally insulated. The initial temperature of all domains is set equal to the corresponding ambient temperature and is used only as the initial value of the steady-state solver. Two separate electrical interfaces are used. In the electrostatics interface, a phase-to-ground voltage of 63.5 kV is applied to the conductor and crimping connector, while the metallic screen is maintained at 0 V. In the electric-currents interface, the root mean square conductor current varies from 400 to 1000 A and is applied at one conductor end, with the opposite terminal grounded. The screen is assumed to be continuously grounded, while sheath circulating currents and cross-bonding effects are not considered.

Specifically, in the electro-thermal coupling model, the cable conductor and metallic shielding layer are treated as conductive materials with temperature-dependent electrical conductivity. The electrical conductivity of the conductor is defined through an analytical function in the finite-element simulation and is expressed as

$$\sigma = \frac{1}{\rho_{\mathrm{red}}[1 + \alpha_{\mathrm{Cu}}(T_{\mathrm{e}} - T_{\mathrm{ref}})]}\, T_e \tag{1}$$

where T_{ref} is the reference temperature, ρ_{red} denotes the electrical resistivity at the reference temperature, α_{Cu} is the temperature coefficient of resistivity for copper, and T_e represents the conductor working temperature.

Following the equivalent heat-source method for cable-joint contact resistance [34], the internal losses are represented by two volumetric heat sources based on the RMS current. The conductor heat source is calculated as

$$G_1 = \frac{I^2\rho}{\pi^2 r^4} \tag{2}$$

where I, ρ and r denote the conductor current, resistivity, and radius, respectively. By defining the equivalent resistivity of the crimping region as $\rho_2 = k_\rho \rho$, the corresponding heat source is expressed as

$$G_2 = k_\rho G_1 \tag{3}$$

In this study, $k_\rho = 5$ follows the representative numerical setting reported in [35] and is treated as a model parameter rather than a measured resistance coefficient for the investigated joint. Therefore, the calculated hotspot temperatures and ampacity values

are specific to this contact-resistance assumption. Metallic-sheath loss, skin effect, and proximity effect are not independently calculated in the present steady-state formulation. Accordingly, the calculated ampacity values are model-specific results under the adopted loss formulation. The dielectric electric field is evaluated using a stationary electrostatic formulation, and dielectric-loss heating is not included in the thermal model.

The electric field is governed by Maxwell's equations under the quasi-static approximation. The governing equations can be written as

$$\nabla \cdot J = 0 \tag{4}$$

$$J = \sigma E \tag{5}$$

$$E = -\nabla V \tag{6}$$

where J is the current density vector, E is the electric field intensity, and V is the electric potential.

The stationary heat transfer within the cable intermediate joint is described by the heat conduction equation,

$$\nabla \cdot \mathbf{q} = Q_{src} \tag{7}$$

where Q_{src} denotes the total heat source applied in the thermal model; $\mathbf{q}$ is the conductive heat flux, which satisfies Fourier's law,

$$\mathbf{q} = -k\nabla T \tag{8}$$

where k is the thermal conductivity; and T is the temperature.

To place the simulated joint thermal behavior in the context of published research, the experimentally validated 110 kV cable-joint study by Liu et al. is considered. Liu et al. validated a finite-element model of a 110 kV cable joint using high-current temperature-rise experiments, with a reported relative calculation error below 6%. They also reported that considering the cable joint reduces the cable-line ampacity by 145 A [36]. This finding is qualitatively consistent with the joint-limited ampacity trend observed in the present simulations. However, differences in joint geometry and installation conditions mean that this comparison provides contextual evidence rather than direct quantitative validation of the present model.

Furthermore, to illustrate the possible influence of the assumed contact-resistance multiplier, a sensitivity analysis is conducted by varying the contact-resistance multiplier from 3 to 7 while keeping the geometry, material properties, boundary conditions, and operating conditions unchanged. The resulting hotspot temperatures at 620 A and 1000 A are compared to assess the influence of the assumed contact-loss parameter. At an ambient temperature of 22 °C, a soil thermal conductivity of 1.1 W/(m·K), and a ground-surface heat-transfer coefficient of 6 W/(m^2·K), the estimated hotspot temperature increases from 43.92 to 45.91 °C at 620 A and from 82.41 to 87.54 °C at 1000 A. The contact-resistance multiplier can influence hotspot temperature when the corresponding contact-loss term is included in the thermal model. Its value should therefore be determined or calibrated for the specific joint geometry and contact conditions in practical applications. In this study, $k_\rho = 5$ is adopted with reference to published numerical studies in [35] rather than experimental calibration of the investigated joint.

2.3. Sensitivity Analysis of Hotspot Temperature Under Multiple Working Conditions

The steady-state hotspot temperature of a buried cable intermediate joint is jointly determined by the electrical loading condition and the surrounding thermal environment. Among the influencing factors, the load current directly governs the magnitude of Joule

heating within the joint and is therefore the dominant factor affecting the internal temperature rise. However, the internal hotspot temperature cannot be measured directly under normal working conditions, making it essential to establish the relationship between the load current and the hotspot temperature for practical ampacity assessment. In addition, the thermal characteristics of the surrounding soil also have a significant influence on heat dissipation. Specifically, the soil thermal conductivity, soil surface heat-transfer coefficient, and ambient temperature affect the overall thermal resistance of the cable system, thereby modifying the temperature distribution within the intermediate joint. These parameters are closely related to installation conditions and environmental variations encountered in practical cable operation. The cable burial depth of 1.0 m, the 4 m × 3 m soil-domain cross-section, and the surface-boundary placement adopted in this study are selected with reference to the three-dimensional directly buried cable-joint model reported by Zhao et al. [37].

To quantitatively evaluate the influence of different working conditions, a one-factor-at-a-time sensitivity analysis is conducted by varying four representative parameters: load current, soil thermal conductivity, soil surface heat-transfer coefficient, and ambient temperature. The corresponding parameter ranges are defined as follows: the load current varied from I = [400–1000] A, the soil thermal conductivity ranged from k_{soil} = [0.5–2.5] W/(m·K), the soil surface heat-transfer coefficient ranged from $H_{soilsurface}$ = [3–12] W/(m^2·K), and the ambient temperature ranged from T_{amb} = [10–40] °C. Within each range, 20 uniformly distributed sample points are selected to perform steady-state electro-thermal simulations, while the remaining parameters are maintained at their reference values. The corresponding simulation results are presented in Figure 4a–d, which illustrate the sensitivity of the hotspot temperature to variations in the four working parameters.

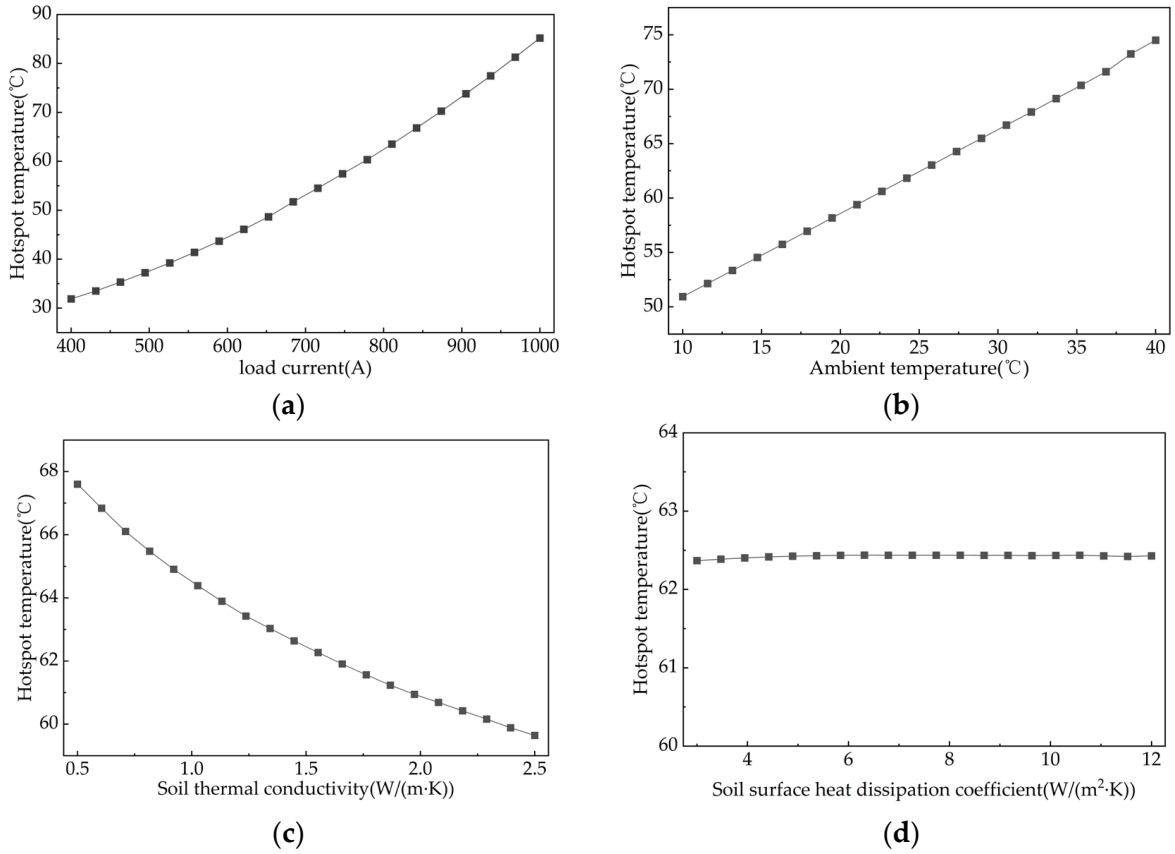

Figure 4. Sensitivity of the hotspot temperature to different working parameters: (**a**) load current; (**b**) ambient temperature; (**c**) soil thermal conductivity; and (**d**) soil surface heat-transfer coefficient.

As shown in Figure 4a, the hotspot temperature increases nonlinearly with load current, consistent with the approximately quadratic dependence of Joule heating on current and the temperature dependence of the material properties. A positive relationship can be observed between the ambient temperature and the hotspot temperature in Figure 4b. An increase in ambient temperature reduces the temperature gradient between the cable system and its surrounding environment, thereby weakening the heat dissipation capability of the joint and resulting in a higher hotspot temperature. As illustrated in Figure 4c, the hotspot temperature decreases with increasing soil thermal conductivity, demonstrating a clear negative correlation. A higher soil thermal conductivity enhances heat transfer from the cable joint to the surrounding soil, thereby reducing thermal resistance and effectively suppressing hotspot formation. In contrast, Figure 4 shows that the hotspot temperature varies by approximately 0.07 °C as the ground-surface heat-transfer coefficient increases from 3 to 12 $W/(m^2 \cdot K)$. To examine whether this weak sensitivity results from the placement of the far-field boundaries, supplementary calculations were performed using soil-domain cross-sections of 2 m × 2 m, 4 m × 3 m, and 8 m × 6 m, while maintaining the burial depth at 1 m and retaining the same material properties and thermal boundary conditions. With uniformly tighter solver settings, the corresponding hotspot-temperature changes were +0.106, +0.113, and −0.045 °C, respectively. The weak sensitivity persisted when the lateral and bottom boundaries were moved both closer to and farther from the cable, indicating that it cannot be attributed simply to excessively distant far-field boundaries. Under the prescribed bottom temperature of 10 °C and ambient air temperature of 25 °C, the ground surface exhibited net heat inflow rather than net heat loss. This supports the interpretation that ground-surface convection is not the dominant outward heat-transfer pathway under the adopted conditions. Nevertheless, boundary placement affected the absolute hotspot temperature, and these results should not be interpreted as demonstrating complete domain independence or generalized to other thermal boundary conditions.

Consequently, under the burial depth, soil-domain dimensions, surface-boundary placement, and parameter ranges adopted in this study, the load current, ambient temperature, and soil thermal conductivity are identified as the main factors affecting the hotspot temperature, whereas the soil surface heat-transfer coefficient shows only a limited influence and is therefore excluded from the subsequent analysis of the present model. This conclusion is model-specific and should be reassessed for other installation conditions.

2.4. Defect Modeling and Electro-Thermal Analysis

2.4.1. Configuration of Typical Insulation Defects

Cable intermediate joints are recognized as one of the most failure-prone components in high-voltage cable systems owing to their complex multilayer structure and field installation process. During manufacturing, installation, and long-term operation, various insulation defects may be introduced or gradually develop, thereby altering the local electro-thermal characteristics of the joint. Among the most common defect types, metallic burrs may remain on the surface of the crimping connector owing to improper conductor crimping, resulting in localized electric field enhancement. Air gaps can be formed when the prefabricated insulation body is not completely bonded to the XLPE insulation, leaving enclosed voids at the insulation interface. Water films may develop as groundwater or soil moisture penetrates the insulation interface during long-term underground service. In addition, prolonged exposure to high electric field stress can progressively initiate water trees, which propagate radially within the insulation and accelerate dielectric degradation. These defects modify the local electric field distribution and heat-transfer paths. Due to this influence, which depends strongly on the defect type, geometry, and location, representative defect models are established to investigate their electro-thermal characteristics systematically.

In this study, four typical insulation defects, namely air gaps, water films, water trees, and metallic burrs, are considered. To establish computationally tractable defect models, simplified three-dimensional geometries are adopted according to the main morphological characteristics of each defect. In particular, the present study focuses on the early-stage morphology of water-tree degradation before extensive branching develops. The water-tree region is therefore represented as an equivalent homogeneous cylindrical moisture-degraded channel oriented along the local electric-field direction. Previous studies have represented water-tree channels or water-tree-degraded regions using cylindrical equivalent geometries for numerical analysis [38,39]. The water tree is represented as an equivalent homogeneous water-filled channel. This treatment is consistent with previous numerical studies that modeled water-tree regions or water-filled voids using water or distilled-water electrical properties. The relative permittivity is set to 80, which is close to the commonly used value of 81 for distilled or deionized water [40]. These simplifications affect the magnitude and location of electric-field peaks by altering defect boundaries and local curvature. They also modify local electrical losses and heat-transfer paths, thereby influencing the temperature distribution and the surface-temperature patterns used for classification. The reported classification performance therefore depends in part on the adopted defect geometries. For water trees, this study focuses on an idealized early stage before extensive branching develops and uses a homogeneous cylindrical channel as an equivalent representation of the localized moisture-degraded region. The material properties, geometries, and locations of the modeled defects are summarized in Table 2a,b, while the locations and geometrical configurations of the defect models are illustrated in Figure 5. All position coordinates refer to the geometric symmetry centers of the defects in the model coordinate system.

Table 2. (**a**). Material properties assigned to the modeled defects. (**b**). Geometry, dimensions, and locations of the modeled defects.

(**a**)

Defect Type	Assigned Material	Electrical Conductivity (S/m)	Density (kg/m^3)	Thermal Conductivity (W/(m·K))	Relative Permittivity
Air gap	Air	1×10^{-18}	1.205	0.026	1
Water film	Water	1×10^{-3}	1000	0.6	80
Water tree	Water	1×10^{-3}	1000	0.6	80
Metallic burr	Copper	5.7×10^{7}	8960	401	1

(**b**)

Defect Type and Material	Geometry and Dimensions	Geometric Center (x, y, z) (mm)	Location
Air gap	Sphere, radius = 3 mm	(0, 0, 48)	Within the joint insulation.
Water film	Thin layer, 24 × 8 × 1 mm	(−12, −4, 69.5)	At the insulation interface near the outer side of the joint.
Water tree	Equivalent homogeneous cylinder, radius = 0.8 mm, length = 18 mm	(0, 0, 52)	Within the insulation, extending toward the outer semiconducting interface.
Metallic burr	Cylinder, radius = 0.9 mm, length = 7 mm	(0, 0, 34)	On the outer surface of the crimping tube, protruding into the insulation.

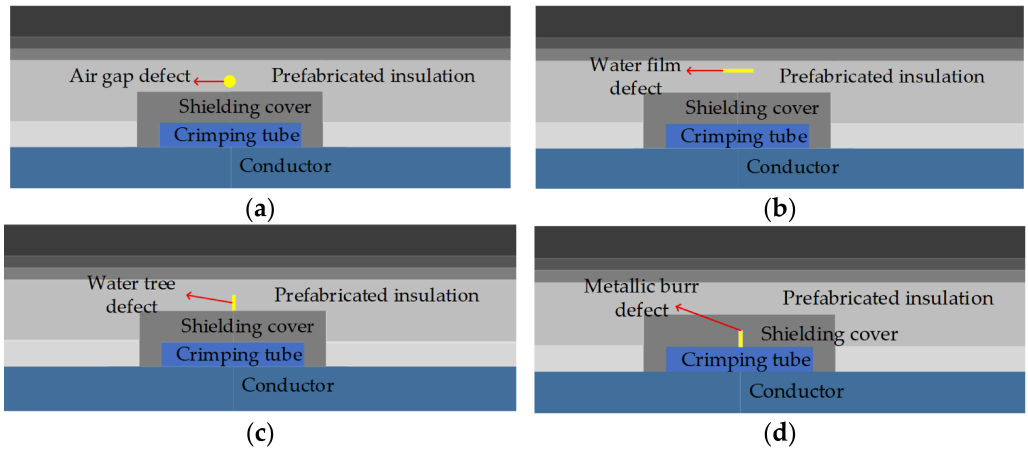

Figure 5. Geometrical configurations and locations of the four representative insulation defects considered in the electro-thermal simulations: (**a**) air gap defect; (**b**) water film defect; (**c**) water tree defect; and (**d**) metallic burr defect.

2.4.2. Temperature Field Analysis Under Different Defect Conditions

To investigate the influence of typical insulation defects on the thermal behavior of cable intermediate joints, the temperature distributions are analyzed from two complementary perspectives: the internal radial temperature distribution and the externally measurable axial surface temperature distribution. This dual-perspective analysis not only reveals the thermal disturbance induced by insulation defects within the joint but also establishes the relationship between internal hotspot characteristics and practical temperature measurements available in field applications.

First, the temperature distribution is extracted along a radial path passing through the defect location. The radial path covers the entire cross-section from the conductor to the outer sheath, and the temperature results are presented in Figure 6. In practical engineering applications, direct temperature measurement inside energized cable joints is difficult to achieve. Therefore, temperature monitoring is typically performed on the outer sheath of the cable joint. In this study, 11 temperature monitoring points are arranged along the axial direction of the outer sheath to simulate practical monitoring conditions. The axial coordinate origin is defined at the center of the joint, and the coordinates of the monitoring points are set as $T_{s1} = -1000$ mm, $T_{s2} = -897.162$ mm, $T_{s3} = -421.803$ mm, $T_{s4} = -308$ mm, $T_{s5} = -238$ mm, $T_{s6} = 0$ mm, $T_{s7} = 238$ mm, $T_{s8} = 308$ mm, $T_{s9} = 437.161$ mm, $T_{s10} = 895.246$ mm, and $T_{s11} = 1000$ mm. These points cover the main thermal regions of the intermediate joint, including the crimping region, stress cone, transition sections, and normal cable body, thereby providing external temperature inputs for subsequent hotspot-temperature inversion and defect identification. The corresponding surface temperature distributions measured at the 11 monitoring locations are presented in Figure 7.

The simulation results show that the four defect types induce localized thermal disturbances near the defect region, leading to slight variations in the internal radial temperature distribution. Among them, the metallic burr produces the most pronounced disturbance due to local electric field enhancement. However, the influence of these defects on the external surface temperature is much weaker. As shown in Figure 7, the surface-temperature perturbations caused by different defects are very small at individual measuring points. Therefore, the present study does not aim to identify the exact defect type from a single temperature measurement. Instead, the 11 axial measuring points are used as a temperature-distribution vector to capture weak spatial pattern changes along the cable joint. It should be noted that these results are obtained from ideal noise-free numerical simulations; under practical measurement conditions, such weak perturbations may be affected by sensor

uncertainty. Accordingly, the subsequent classification results quantify the numerical separability of the simulated surface-temperature patterns rather than verified defect-detection performance under practical sensor conditions.

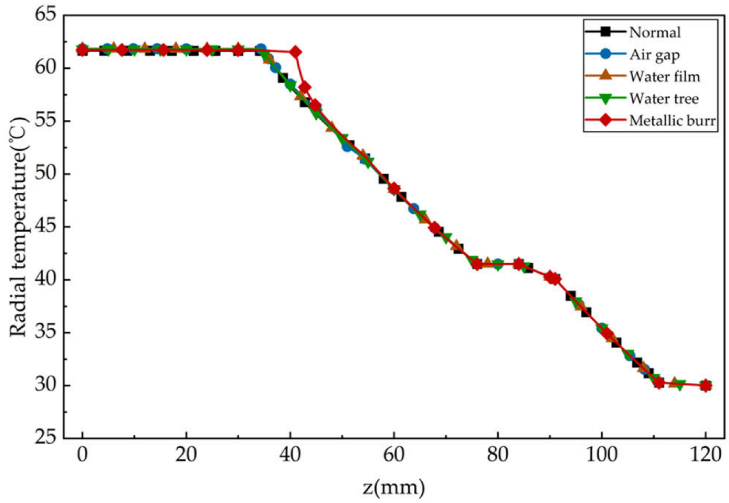

Figure 6. Radial temperature distributions along the defect locations for different defect conditions.

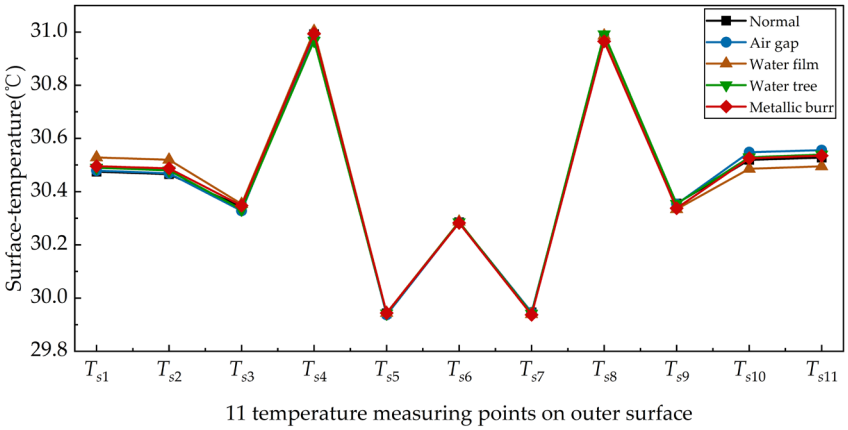

Figure 7. Surface temperature distributions at the 11 monitoring points of the cable intermediate joint under different defect conditions.

2.4.3. Defect-Dependent Electric-Field Distortion Analysis

Insulation defects can affect both the temperature distribution and the local electric-field characteristics. In the present model, the thermal field is calculated from resistive heat sources and heat conduction, while the dielectric electric field is evaluated using a stationary electrostatic formulation. Electric-field distortion is analyzed separately as an indicator of local electrical stress and is not coupled into the thermal model through dielectric-loss heating. All electric-field quantities reported in Figure 8 and used in the heuristic derating coefficient are the electric-field magnitudes sampled along the prescribed radial path. The reported radial-path values are generated at I = 800 A, T_{amb} = 25 °C, k_{soil} = 1.5 W/(m·K), H = 6 W/(m^2·K), and 63.5 kV phase-to-ground voltage using the saved finer mesh. As shown in Figure 8, the radial-path electric field peaks are 3.021, 2.988, 3.072, 6.391, and 3.046 MV/m for the healthy, air-gap, water-film, equivalent water-tree, and metallic-burr models, respectively. Compared with the temperature-field results, the electric field shows much higher sensitivity to insulation defects. Although these defects cause only slight hotspot-temperature variations and negligible surface temperature responses, they can lead

to significant local electric-field enhancement. Such field concentration may accelerate insulation aging, promote partial discharge, and increase the risk of dielectric breakdown under long-term operation. Therefore, temperature-based assessment alone is insufficient for assessing the operating safety of cable intermediate joints. The insulation defect state should be incorporated into hotspot-temperature inversion and ampacity assessment, providing the physical basis for the proposed defect-aware ampacity assessment framework.

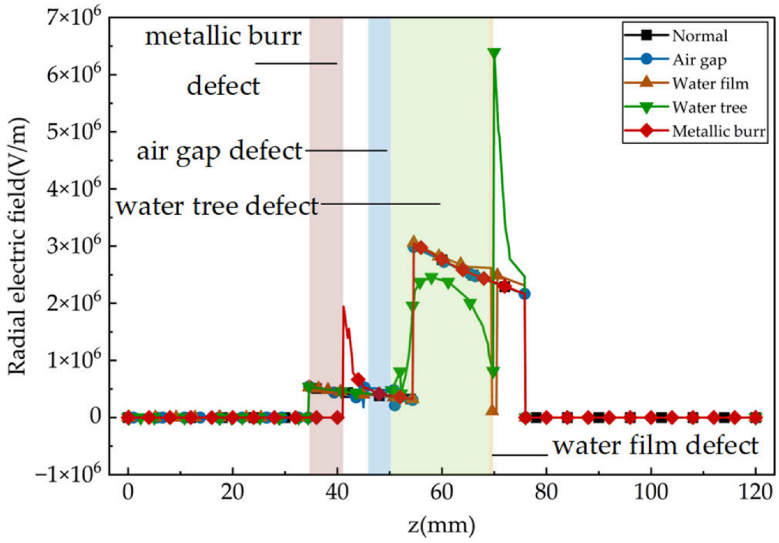

Figure 8. Radial electric field profiles along the defect locations under different defect conditions.

2.4.4. Numerical Sensitivity of Electric-Field Extraction

To evaluate the numerical stability of the hotspot temperature and electric-field extraction, a three-level mesh sensitivity analysis is performed for the healthy joint and the equivalent water-tree case under identical geometrical, material, electrical, and environmental conditions, and the results are summarized in Table 3. The mesh-refinement results show that the hotspot temperature is numerically stable, with changes of only 0.767% and 0.444% between the finer and extra-fine meshes for the healthy and water-tree cases, respectively. In contrast, the pointwise global maximum electric field remains highly sensitive to mesh refinement, whereas the prescribed radial-path peak shows substantially better stability, with corresponding changes of 0.236% and 15.52%. Although the radial-path extraction is less sensitive than the whole-model pointwise maximum in this comparison, the water-tree result still exhibits appreciable mesh dependence. Its effect on the heuristic derating coefficient is quantified in Section 3.2. These results indicate that the whole-model pointwise maximum is strongly affected by local discretization near the defect interface.

Table 3. Mesh sensitivity of hotspot temperature and electric-field extraction.

Case	Mesh	Elements	Nominal Global h_{min} Setting (mm)	T_{max} (°C)	Global E_{max} (MV/m)	Path E_{peak} (MV/m)
Healthy	Fine	90,488	40	81.652	129.824	2.973
Healthy	Finer	245,579	16	62.464	66.208	3.021
Healthy	Extra fine	1,172,557	6	62.943	6.288	3.028
Water tree	Fine	94,900	40	80.709	35.929	5.825
Water tree	Finer	249,213	16	62.633	2658.842	6.391
Water tree	Extra fine	1,179,758	6	62.911	13.671	7.383

Although the hotspot-temperature results show relatively small variations under mesh refinement, the much smaller defect-induced surface-temperature differences remain sensitive to mesh discretization. To further examine the influence of the simplified water-tree representation, a numerical sensitivity analysis is performed by perturbing the relative permittivity and electrical conductivity of the equivalent degraded region around their baseline values. The results are summarized in Table 4.

Table 4. Sensitivity of the equivalent water-tree representation to electrical material parameters.

Case	ε_r	σ (S/m)	T_{max} (°C)	Path E_{peak} (MV/m)
Baseline	80	1×10^{-3}	62.598	6.391
Lower ε_r	40	1×10^{-3}	62.598	4.989
Higher ε_r	120	1×10^{-3}	62.598	7.535
Lower σ	80	1×10^{-4}	62.598	6.391
Higher σ	80	1×10^{-2}	62.598	6.391

Within the tested range, changing the relative permittivity from 40 to 120 changes the maximum electric field along the selected radial path from 4.989 MV/m to 7.535 MV/m, corresponding to approximately 77.7–117.4% of the baseline value. By contrast, varying the electrical conductivity from 10^{-4} to 10^{-2} S/m produces negligible changes in the reported steady-state quantities under the present modeling conditions. These results indicate that the absolute magnitude of the local electric-field enhancement depends on the assumed effective dielectric properties of the equivalent defect region, although localized field redistribution remains evident. Accordingly, the water-tree region used in this study is regarded as an equivalent moisture-degraded region rather than a detailed representation of the microscopic branched morphology of an actual water tree.

3. Defect-Aware Hotspot-Temperature Inversion and Ampacity Margin Assessment

3.1. Defect-Aware Hotspot-Temperature Inversion Model

3.1.1. Gaussian-Kernel Inversion Framework

The proposed Gaussian-kernel inversion framework consists of two related components. Hotspot temperature is estimated using Gaussian process regression (GPR), whereas defect-state identification is performed using a logistically calibrated Gaussian-kernel ridge classifier. The two components use the same standardized input features and RBF kernel but are trained using separate target variables. The defect classifier is not a standard Gaussian process classifier because it does not employ a Bernoulli likelihood or posterior approximation.

For hotspot-temperature inversion, let $X = [x_1, x_2, \ldots, x_n]^{\mathrm{T}}$ denote the standardized training input matrix, where x_i is the d-dimensional feature vector of the i-th training sample, and n is the number of training samples. Let $X = [x_1, x_2, \ldots, x_n]^{\mathrm{T}}$ $y_{\mathrm{T}} = [y_1, y_2, \ldots, y_n]^{\mathrm{T}}$ denote the standardized hotspot-temperature vector obtained from simulations. The covariance between two input samples is described by the RBF kernel,

$$k(x_i, x_j) = \sigma_{\mathrm{f}}^2 \exp\left(-\frac{\|x_i - x_j\|^2}{2l^2}\right) \tag{9}$$

where σ_{f}^2 is the signal variance, l is the kernel length scale, which controls the smoothness of the nonlinear mapping, and $\|x_i - x_j\|$ denotes the Euclidean distance between two standardized feature vectors. The training covariance matrix is then written as

$$K_{\mathrm{T}} = K(X, X) + \sigma_{\mathrm{n}}^2 I \tag{10}$$

where $K(X,X)$ is the n × n covariance matrix with its (i,j)-th element equal to $k(x_i,x_j)$, σ_n^2 is the observation-noise variance, and I is the identity matrix. In this work, σ_f^2 is set to 1, σ_n^2 is set to 10^{-4}, and an additional jitter term of 10^{-9} is added to the diagonal of K_T for numerical stability. The length scale l is selected as the median distance estimated from randomly sampled pairs of standardized training samples.

For a test sample x_*, the covariance vector between x_* and the training samples is defined as

$$k_* = k(x_*,X) = [k(x_*,x_1),k(x_*,x_2),\ldots,k(x_*,x_n)] \tag{11}$$

The predictive mean of the standardized hotspot temperature is obtained as

$$\mu_T(x_*) = k_* K_T^{-1} y_T \tag{12}$$

In the implementation, the matrix inverse is not computed explicitly; instead, Cholesky decomposition is used to solve the linear system for the predictive mean. The predicted hotspot temperature in the original physical space is recovered through inverse normalization,

$$T_{\text{hot,pred}} = \mu_T(x_*)\sigma_y + \mu_y \tag{13}$$

where μ_y and σ_y are the mean and standard deviation of the hotspot temperature in the training dataset, respectively.

For defect-state identification, given the binary training labels y_{cls}, the classification weight vector α_{cls} is obtained by minimizing

$$\min_{f\in\mathcal{H}} \sum_{i=1}^{n} \left[y_{\text{cls},i} - f(x_i)\right]^2 + \lambda_{\text{cls}}\|f\|_{\mathcal{H}}^2 \tag{14}$$

where λ_{cls} is the regularization parameter, fixed at 10^{-4}, and $\mathcal{H}$ denotes the reproducing-kernel Hilbert space associated with the RBF kernel. The corresponding classification weight vector is

$$\alpha_{\text{cls}} = (\mathrm{K} + \lambda_{\text{cls}} I)^{-1} y_{\text{cls}} \tag{15}$$

where K is the Gaussian-kernel matrix. The resulting linear system is solved using Cholesky decomposition with a small diagonal jitter for numerical stability. For defect-state identification, the latent classification score is calculated as

$$f_\theta(x_*) = k_*^{\mathrm{T}} \alpha_{\text{cls}} \tag{16}$$

where α_{cls} represents the classification weight vector and k_*^{T} denotes the Gaussian-kernel vector between the input sample and all training samples. The latent score is then converted into a defect probability using logistic calibration,

$$p_\theta(x_*) = P(\theta = 1|x_*) = \frac{1}{1 + \exp[-(af_\theta(x_*) + b)]} \tag{17}$$

where a and b are calibration parameters estimated from out-of-fold latent scores generated within the training data and are kept fixed during testing. Five training folds are used so that each calibration score is produced by a classifier that did not use that sample for fitting. The insulation state is determined as

$$\theta = \begin{cases} 1, & p_\theta(x_*) \geq 0.5 \\ 0, & p_\theta(x_*) < 0.5 \end{cases} \tag{18}$$

where 0 and 1 denote the healthy and defective states, respectively. The same out-of-fold logistic-calibration procedure and a probability threshold of 0.5 are used for the reported Gaussian-kernel classification experiments.

Considering that the surface-temperature perturbations produced by the modeled defects are small, the present study formulates defect identification as a binary healthy/defective problem rather than attempting to distinguish individual defect types. The full 11-point axial temperature vector and engineered distribution descriptors are used instead of an isolated temperature measurement. The noise-free classification results quantify numerical separability within the simulated dataset; their sensitivity to surface-temperature measurement uncertainty is evaluated in Section 3.1.6.

3.1.2. Input Feature Construction for the Gaussian-Kernel Framework

The Gaussian-kernel inversion framework adopts a 25-dimensional input feature vector to characterize the operating and thermal state of the cable intermediate joint. In addition to the eleven surface temperatures measured along the outer sheath, fourteen auxiliary features are constructed, including the load current, ambient temperature, soil thermal conductivity, and eleven engineered descriptors derived from the surface temperature distribution. These derived features are designed to quantify the global temperature level, spatial non-uniformity, localized thermal variation, and electro-thermal operating condition of the joint. They provide information derived from the original pointwise temperature measurements and enhance the robustness of hotspot-temperature inversion and defect-state identification. The mathematical definitions of the engineered features are given as follows.

1. Mean surface temperature

   The average temperature of the surface monitoring points is defined as

$$T_{\mathrm{s,mean}} = \left(\frac{1}{n}\right) \times \sum_{i=1}^{n} \left(T_{\mathrm{s}_i}\right) \tag{19}$$

   where T_{s_i} denotes the temperature measured at the i-th monitoring location. This feature represents the overall thermal level of the cable joint surface.

2. Standard deviation of surface temperature

   The standard deviation is calculated as

$$T_{\mathrm{s,std}} = \sqrt{\frac{1}{n}\sum_{i=1}^{n} \left(T_{\mathrm{s}_i} - T_{\mathrm{s,mean}}\right)^2} \tag{20}$$

   which quantifies the spatial dispersion of the surface temperature distribution. Larger values indicate stronger temperature non-uniformity and more pronounced local thermal concentration.

3. Minimum surface temperature

   The minimum temperature is given by

$$T_{\mathrm{s,min}} = \min\left(T_{\mathrm{s}_i}\right) \tag{21}$$

4. Maximum surface temperature

   The maximum temperature is given by

$$T_{\mathrm{s,max}} = \max\left(T_{\mathrm{s}_i}\right) \tag{22}$$

where $T_{\mathrm{s,min}}$ provides the baseline surface temperature and $T_{\mathrm{s,max}}$ represents the highest externally observable thermal response of the cable joint.

5. Surface temperature range

The temperature range is defined as

$$T_{\mathrm{s,range}} = T_{\mathrm{s,max}} - T_{\mathrm{s,min}} \tag{23}$$

which characterizes the overall fluctuation of the surface temperature field and reflects the degree of temperature non-uniformity along the cable joint.

6. Temperature rise at the cable joint center

The temperature difference between the central monitoring point and the average temperature of the two terminal monitoring points is calculated as

$$T_{\mathrm{s,center\text{-}minus\text{-}edge}} = T_{\mathrm{s}_6} - \frac{T_{\mathrm{s}_1} + T_{\mathrm{s}_{11}}}{2} \tag{24}$$

where T_{s_6} corresponds to the monitoring point located at the crimping region. This feature describes the localized heat accumulation around the joint center and reflects the thermal concentration caused by conductor connection losses.

7. Mean temperature rise relative to ambient

The average temperature rise relative to the ambient temperature is defined as

$$T_{\mathrm{s,rise\text{-}mean}} = T_{\mathrm{s,mean}} - T_{\mathrm{amb}} \tag{25}$$

which removes the influence of ambient temperature and characterizes the overall heating intensity of the cable joint.

8. Maximum temperature rise relative to ambient

The maximum temperature rise is calculated as

$$T_{\mathrm{s,rise\text{-}max}} = T_{\mathrm{s,max}} - T_{\mathrm{amb}} \tag{26}$$

representing the highest observable thermal anomaly relative to the surrounding environment.

9. Axial temperature gradient

The axial temperature gradient is defined as

$$T_{\mathrm{s,axial\text{-}gradient}} = T_{\mathrm{s}_{11}} - T_{\mathrm{s}_1} \tag{27}$$

which reflects the temperature difference between the two ends of the cable joint and can be used to identify asymmetric thermal distributions along the axial direction.

10. Squared load current

Considering that Joule heating is proportional to the square of the load current, the following feature is introduced as

$$I_{\mathrm{squared}} = I^2 \tag{28}$$

which directly represents the heat generation intensity of the conductor.

11. Electro-thermal coupling indicator

To jointly characterize electrical loading and soil heat dissipation capability, the following physics-informed feature is defined as

$$I_{\mathrm{squared,over\text{-}k\text{-}soil}} = \frac{I^2}{k_{\mathrm{soil}}} \tag{29}$$

where k_{soil} denotes the soil thermal conductivity. This feature represents the combined influence of Joule heating and surrounding heat dissipation capacity. Larger values indicate higher internal overheating risk caused by stronger heat generation and poorer thermal conduction.

The constructed features include statistical descriptors, spatial temperature-distribution characteristics, and physics-informed electro-thermal variables, which together characterize the operating state of the cable intermediate joint. The input feature matrix is defined as $X \in R^{N\times 25}$, where N denotes the number of samples and each sample contains 25 input features, $[T_{s1},T_{s2},\ldots,T_{s11},I,T_{amb},k_{soil},T_{s,mean},T_{s,std},\ldots,I_{squared,over\text{-}k\text{-}soil}]$. Since these variables possess different physical units and numerical scales, feature standardization is performed prior to model training. Each feature is normalized as

$$X_s = \frac{X - \mu_x}{\sigma_x} \tag{30}$$

where μ_x and σ_x denote the mean and standard deviation of each feature calculated from the training dataset, respectively. After normalization, all features have zero mean and unit variance, ensuring balanced contributions during kernel distance calculation.

3.1.3. Inversion Performance Evaluation Metrics

To quantitatively evaluate the performance of the proposed hotspot-temperature inversion model, three widely used regression error metrics are adopted: the mean absolute error (MAE), root mean square error (RMSE), and maximum absolute error (MaxAE). These metrics comprehensively assess the average prediction accuracy, overall error distribution, and worst-case prediction performance, respectively. Their mathematical definitions are given as follows:

$$\mathrm{MAE} = \frac{1}{n}\sum_{i=1}^{n}\left|T_p - T_i\right| \tag{31}$$

$$\mathrm{RMSE} = \sqrt{\frac{1}{n}\sum_{i=1}^{n}\left(T_p - T_i\right)^2} \tag{32}$$

$$\mathrm{MaxAE} = \max_{1\le i\le n}|T_p - T_i| \tag{33}$$

where n denotes the number of testing samples, T_p is the predicted hotspot temperature, and T_i is the corresponding reference value obtained from the electro-thermal simulations.

For the binary defect classification task, the classification accuracy is employed to evaluate the defect identification performance of the proposed model.

3.1.4. Model Comparison and Performance Analysis

To validate the effectiveness of the proposed method, a simulation dataset containing 1600 samples is used, including 800 defect-free samples and 800 defective samples. The defective samples consist of four insulation defect types, namely air gaps, water films, water trees, and metallic burrs, with 200 samples for each defect type. For both healthy and defective samples, the load current, ambient temperature, and soil thermal conductivity are independently generated using Latin hypercube sampling with identical parameter ranges of 400–1000 A, 10–40 °C, and 0.5–2.5 W/(m·K), respectively. For each variable, its prescribed range is first divided into the same number of equal intervals. One value is then selected from each interval, and the sampled values of different variables are independently shuffled and combined to form the dataset. The dataset is randomly divided into training and testing subsets at a ratio of 8:2, yielding 1280 training samples and 320 testing samples. Two representative machine learning models, ridge regression (RR) and back propagation neural network (BPNN), are selected for comparison. RR represents a typical linear regression method, whereas BPNN represents a nonlinear data-driven model widely used for temperature prediction. The structures of the three employed models are illustrated in Figure 9. For RR, hotspot temperature is predicted by ridge regression with the ridge regularization parameter set to 10^{-2}. For binary defect classification, the ridge output is

treated as a latent defect score, converted into a probability through logistic calibration, and thresholded at 0.5. For BPNN, a shared fully connected network with three hidden layers of 96, 64, and 32 neurons is used, followed by one regression head for hotspot temperature and one classification head for defect state. ReLU activation is adopted, with a dropout rate of 0.05 in the grouped cross-validation experiments. The optimizer is AdamW with a learning rate of 2×10^{-3} and a weight decay of 10^{-4}. The learning rate is multiplied by 0.25 after 60% of the epochs. For the primary 80/20 comparison, BPNN is trained for 1200 epochs using full-batch optimization (batch size 1280), without dropout or early stopping. The loss combines standardized-hotspot-temperature MSE and binary cross-entropy with logits, weighted by 1 and 0.4, respectively. These hyperparameters are fixed settings rather than the outcome of a systematic hyperparameter search. In five supplementary reruns using five different seeds, BPNN achieves an MAE of 0.2448 ± 0.0117 °C and an accuracy of 92.38 ± 0.52% (mean ± sample standard deviation). The Gaussian model retains lower observed MAE and higher accuracy across these runs, although statistical superiority is not established for every initialization.

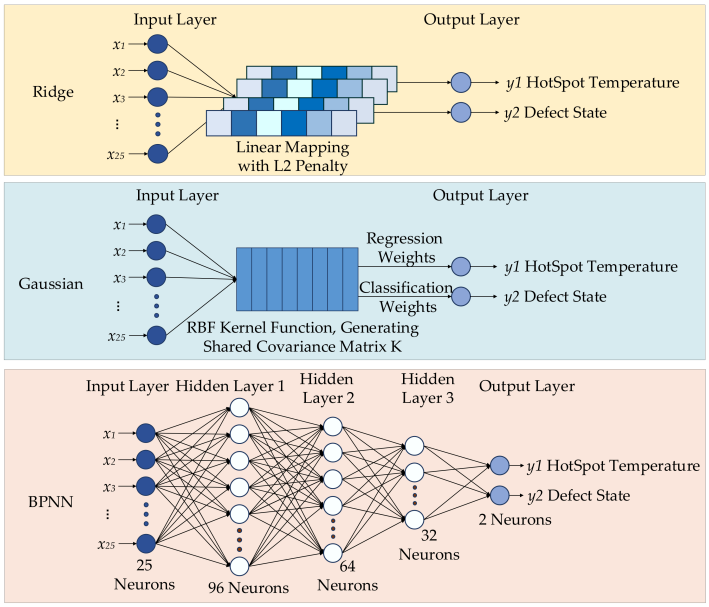

Figure 9. Comparison of the three inversion model architectures.

The proposed Gaussian-kernel framework combines GPR-based hotspot-temperature prediction with calibrated Gaussian-kernel ridge classification. By using a shared RBF kernel, the two tasks exploit the same feature-space similarity while maintaining separate prediction objectives. Compared with BPNN, the Gaussian-kernel framework avoids complex network design and provides more stable nonlinear modeling capability for small- and medium-sized datasets. The architectures of the three models are presented in Figure 9, and the quantitative performance comparison of the three models for hotspot-temperature inversion and defect classification is presented in Table 5.

Table 5. Performance comparison of the three inversion models on the testing dataset.

Model	MAE (°C)	RMSE (°C)	MaxAE (°C)	Defect Classification Accuracy (%)
Ridge	0.108	0.132	0.374	89.06%
Gaussian	0.075	0.116	0.870	95.31%
BPNN	0.250	0.332	1.323	91.88%

As shown in Table 5, the proposed Gaussian-kernel framework achieves the best overall performance among the three inversion models. For hotspot-temperature inversion, the GPR component obtains the lowest MAE and RMSE, which are 0.075 °C and 0.116 °C, respectively, indicating the smallest average prediction error and overall deviation. In addition, it achieves a defect classification accuracy of 95.31%, outperforming RR and the BPNN, whose classification accuracies are 89.06% and 91.88%, respectively. Although RR yields the smallest maximum absolute error, its higher MAE and RMSE suggest that the linear mapping assumption limits its ability to capture the nonlinear electro-thermal behavior of cable intermediate joints. The BPNN can represent nonlinear relationships, but its larger prediction errors indicate reduced stability under the limited training data used in this study. It is noted that the reported classification accuracy is obtained from ideal noise-free numerical simulations and should be interpreted as numerical separability rather than guaranteed field detectability under realistic measurement noise.

The error distributions in Figure 10 further confirm the superior hotspot-temperature inversion performance of the GPR component. As shown in Figure 10a, the GPR component exhibits the most concentrated absolute error distribution, with a median absolute error of approximately 0.049 °C and a smaller interquartile range than those of RR and BPNN. This indicates that the GPR component provides more stable predictions for most testing samples. In contrast, RR shows larger median and upper-quartile errors, while BPNN presents a wider error distribution, reflecting greater prediction dispersion under different operating conditions. The error histograms in Figure 10b show that the prediction errors of the GPR component are closely centered around zero, with a sharper peak and narrower distribution. Overall, the proposed Gaussian-kernel framework achieves higher regression accuracy, better defect-state identification performance, and more stable prediction behavior than the compared models. Therefore, the proposed Gaussian-kernel framework provides a more reliable basis for subsequent defect-aware ampacity margin assessment of cable intermediate joints.

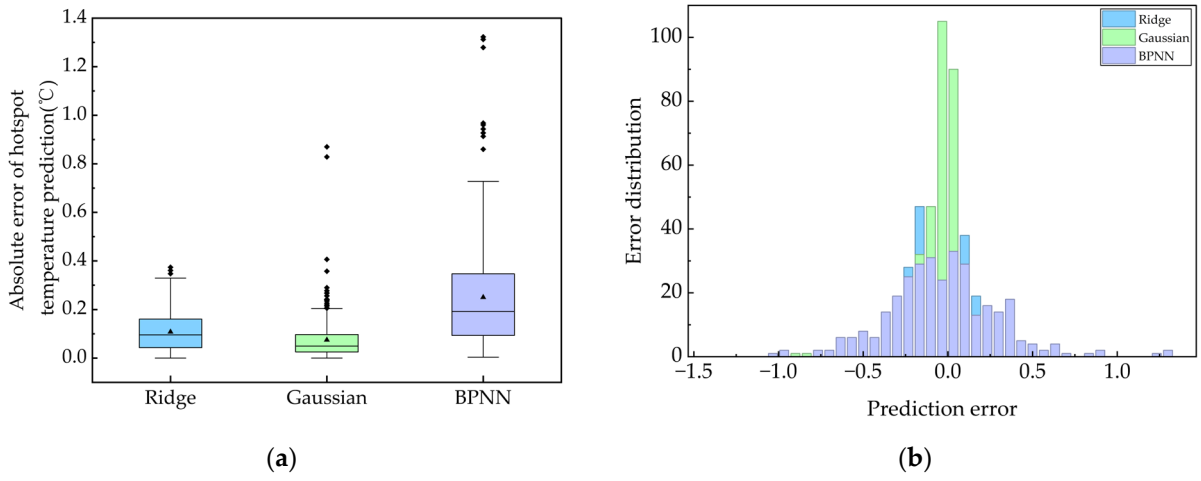

Figure 10. Comparison of hotspot-temperature prediction errors of the three inversion models on the testing dataset: (**a**) boxplot of absolute prediction errors; (**b**) histogram of prediction error distribution.

Note: In the following figures and tables, "Gaussian" denotes the combined GPR and logistically calibrated Gaussian-kernel ridge models.

To provide a more complete assessment of binary defect detection, recall, specificity, precision, F1 score, area under the curve (AUC), and the false-negative rate (FNR) are calculated on the original 320-sample testing subset. The corresponding results are summarized in Table 6. The comparison results of the three models are shown in Figure 11, and

the detection performance of the calibrated Gaussian-kernel ridge classifier for individual defect types is presented in Table 7.

Table 6. Binary defect-detection performance on the original testing subset.

Model	Accuracy	Recall	Specificity	Precision	F1	AUC	FNR
Ridge	0.8906	0.8698	0.9139	0.9188	0.8936	0.9513	0.1302
Gaussian	0.9531	0.9349	0.9735	0.9753	0.9547	0.9842	0.0651
BPNN	0.9188	0.8817	0.9603	0.9613	0.9198	0.9816	0.1183

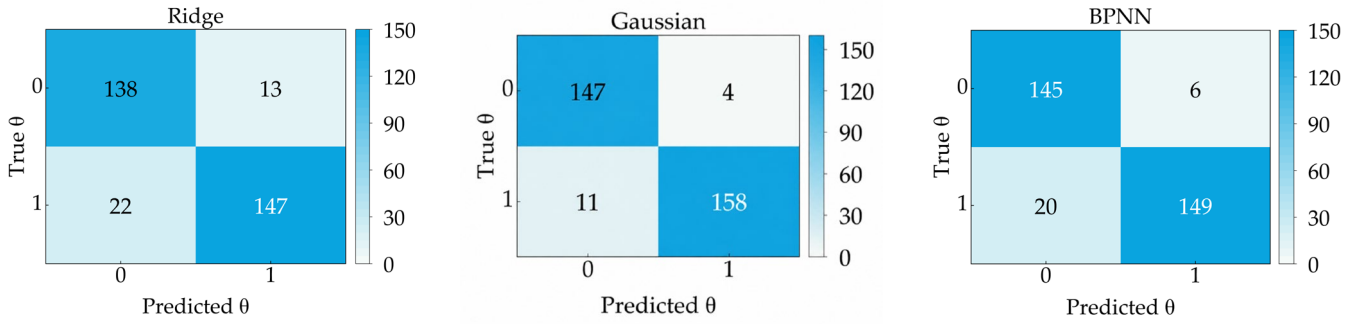

(**a**) Ridge (**b**) Gaussian (**c**) BPNN

Figure 11. Confusion matrices for binary defect detection on the original testing subset.

Table 7. Detection performance of the calibrated Gaussian-kernel ridge classifier for individual defect types.

Defect Type	Recall	FNR
Air gap	0.8261	0.1739
Water film	1.0000	0.0000
Water tree	0.9231	0.0769
Metallic burr	1.0000	0.0000

After out-of-fold logistic calibration, the Gaussian-kernel classifier achieves an accuracy of 0.9531, a recall of 0.9349, a specificity of 0.9735, an AUC of 0.9842, and an FNR of 0.0651 on the original testing subset. Water-film and metallic-burr cases are completely detected in this subset, while air-gap and water-tree cases have recalls of 0.8261 and 0.9231, respectively. Because each defect type uses a fixed reference geometry in the original dataset, the 95.31% accuracy characterizes noise-free within-configuration discrimination rather than generalization to unseen defect geometries.

3.1.5. Feature Ablation Study

To verify the effectiveness of the engineered features, four groups of different inputs are used to train the Gaussian-kernel inversion framework. First Group: eleven outer sheath temperature measurement points, I, T_{amb} and k_{soil}; Second Group: the First Group plus I_{squared} and $I_{\text{squared,over-k-soil}}$; Third Group: the First Group supplemented with statistical features of temperature distribution: $T_{\text{s,mean}}$, $T_{\text{s,std}}$, $T_{\text{s,min}}$, $T_{\text{s,max}}$, $T_{\text{s,range}}$, $T_{\text{s,center-minus-edge}}$, $T_{\text{s,rise-mean}}$, $T_{\text{s,rise-max}}$, $T_{\text{s,axial-gradient}}$; Fourth Group: all 25 features. Feature selection follows a hierarchical multi-objective criterion. Classification accuracy and FNR are considered first. Among the models with the best classification performance, MAE evaluates average prediction accuracy, while maximum absolute error evaluates worst-case stability. The comparison results are shown in Table 8.

Table 8. Gaussian-kernel model feature ablation results on the original testing subset.

Feature Group	Number of Features	Hotspot MAE (°C)	RMSE (°C)	Maximum Error (°C)	Classification Accuracy	FNR	AUC
First Group	14	0.0804	0.1098	0.4133	0.9531	0.0769	0.9936
Second Group	16	0.0833	0.1120	0.4013	0.9438	0.0888	0.9911
Third Group	23	0.0735	0.1088	0.9391	0.9531	0.0769	0.9851
Fourth Group	25	0.0746	0.1158	0.8700	0.9531	0.0651	0.9842

Table 8 presents a comparative ablation analysis of four feature groups. The First Group achieves a classification accuracy of 0.9563 and an FNR of 0.0592, compared with 0.9531 and 0.0651 for the Fourth Group, respectively. The First Group obtains a higher AUC and a lower maximum absolute error, but its MAE reaches 0.0804 °C. The Third Group achieves the lowest MAE and RMSE, but its maximum error increases to 0.9391 °C. The Fourth Group achieves an MAE of 0.0746 °C, only 0.0011 °C higher than that of the Third Group, while reducing the maximum error to 0.8700 °C. It should be emphasized that the complete 25-feature representation is predefined before the ablation study rather than selected based on the test-set results. Therefore, the ablation study serves to evaluate the relative performance of different feature representations rather than to determine the optimal feature group. The results indicate that the 25-feature representation does not consistently outperform the simpler alternatives. In particular, the First Group achieves better classification performance and maximum-error control, whereas the Fourth Group provides a lower average hotspot-temperature prediction error than the First Group.

3.1.6. Surface-Temperature Measurement-Noise Sensitivity

To evaluate whether the numerical defect separation persists under measurement uncertainty, independent zero-mean Gaussian perturbations are added to the 11 surface-temperature inputs and each nonzero noise level is repeated 30 times. Without added noise, hotspot MAE, classification accuracy, recall, and FNR are 0.0746 °C, 0.9531, 0.9349, and 0.0651, respectively. At a noise standard deviation of 0.05 °C, the corresponding mean values become 0.6313 °C, 0.5142, 0.5203, and 0.4797; at 0.10 °C, they become 2.0365 °C, 0.4922, 0.4209, and 0.5791. The marked degradation in both hotspot-temperature prediction and defect classification indicates that the noise-free classification result represents numerical separability under ideal simulation conditions and should not be interpreted as evidence of practical defect-detection capability under measurement uncertainty. Sensor calibration, quantization, long-term drift, sensor-placement error, thermal-contact variability, and model–field discrepancy require further experimental assessment. The increased false-negative rate under measurement noise indicates that some defective joints may be incorrectly classified as healthy, thereby preventing the activation of the heuristic derating rule and resulting in the application of the unadjusted thermal current limit. This limitation highlights the need for improved noise robustness before practical application. Furthermore, when developing simulation-based models for actual cable joints, a comprehensive range of potential defect types, sizes, and locations should be considered to improve the representativeness of the training dataset and the model's adaptability to practical operating conditions.

3.2. Defect-Aware Ampacity Margin Assessment

After the internal hotspot temperature is estimated from externally measured surface temperatures, it is further used to evaluate the steady-state ampacity margin of the cable intermediate joint. Since surface temperature measurements are insufficient for reliably

distinguishing specific defect types, the proposed method does not perform multi-class defect identification; instead, the joint condition is classified into two operating states, namely healthy and defective, according to the output of the calibrated Gaussian-kernel ridge classifier. For a given working current, the externally measured surface temperatures, together with the ambient temperature and soil thermal conductivity, are input into the trained Gaussian-kernel framework to estimate the hotspot temperature and the corresponding defect state. Subsequently, the allowable ampacity is determined according to the identified working condition. When the cable joint is classified as healthy, the maximum allowable current is directly obtained from the binary-search procedure under the hotspot-temperature limit of 90 °C. The 90 °C limit corresponds to the maximum continuous operating temperature of the XLPE insulation system. In this study, it is applied to the maximum temperature in the conductor–crimping connector region, where the hotspot occurs. It should be noted that the 90 °C criterion does not exceed the temperature ratings of the materials constituting the investigated joint: XLPE insulation is rated for a maximum continuous conductor temperature of 90 °C, the semiconductive screens share the same temperature class, and the silicone-rubber material of the prefabricated insulation and stress-cone bodies is a high-temperature elastomer with a typical continuous-service rating of approximately 180 °C, whereas the prefabricated accessories themselves are rated for the same 90 °C system temperature class as the cable. Because the hotspot is located in the conductor–crimping connector region, enforcing the 90 °C limit at this location conservatively bounds the temperatures of all neighboring insulation materials, which remain below the hotspot value in the simulations. When a defect is detected, the allowable ampacity is reduced by introducing a heuristic derating coefficient, yielding

$$I_{allow}^{\max} = \begin{cases} I_{\text{search}}^{max}, \theta = 0 \\ k_d I_{\text{search}}^{max}, \theta = 1 \end{cases} \tag{34}$$

where $I_{allow}^{\max}$ is the allowable ampacity; I_{search}^{max} is the healthy-state ampacity determined by the bisection search under the hotspot-temperature limit of 90 °C; θ denotes the predicted defect state, with $\theta = 0$ representing a healthy joint and $\theta = 1$ indicating a defective joint; and k_d is the defect-aware reduction coefficient, which is defined as

$$k_{d,i} = \min_i(k_{d,i}), \quad k_{d,i} = \frac{1}{1+0.1\max\left(\ln \frac{E_i^{\max}}{E_{normal}^{max}}, 0\right)} \tag{35}$$

where $E_i^{\max}$ is the maximum electric-field magnitude sampled along the prescribed radial path for defect i and E_{normal}^{max} is the corresponding healthy-model value. The logarithmic transformation, positive-part operator, and factor 0.1 are empirical choices introduced solely to construct an illustrative heuristic derating rule; they are not derived from an established dielectric-design criterion, insulation-lifetime model, or experimentally validated safety threshold. Because the binary classifier identifies only the presence of a defect without determining its specific type, a defect-specific coefficient is first calculated for each modeled defect, and the common coefficient is selected as the most conservative value among the four cases rather than their arithmetic average. Using the maximum electric field along the selected radial path of 3.021, 2.988, 3.072, 6.391, and 3.046 MV/m for the healthy, air-gap, water-film, water-tree, and metallic-burr models, respectively, the corresponding defect-specific coefficients are 1.000, 0.9983, 0.9303, and 0.9992. Therefore, $k_{\text{d}} = 0.9303$, corresponding to the smallest coefficient among the four original defect cases evaluated using the finer mesh, is adopted as the baseline illustrative heuristic derating coefficient. Using the paired healthy and water-tree radial-path peaks in Table 3, Equation (35) gives a derating coefficient of approximately 0.9303 for the finer mesh and 0.9182 for the extra-fine mesh, corresponding to a relative decrease of approximately 1.30%. At a fixed thermal-limit current of 983.59 A, the corresponding adjusted currents are approximately 915.03 A

and 903.10 A, respectively, a difference of 11.93 A. These calculations use the coefficients before rounding. The logarithmic mapping therefore attenuates, but does not eliminate, the influence of electric-field mesh sensitivity on the adjusted current. The coefficient of 0.9303 is retained as the baseline illustrative parameter associated with the original finer-mesh results, rather than as a mesh-independent or physically validated safety factor. The proposed derating coefficient is an illustrative heuristic intended to represent a defect-related current adjustment based on simulated electric-field distortion. It is not derived from a validated thermal or dielectric failure criterion and therefore should not be interpreted as a physically established safe operating current limit.

The overall workflow is illustrated in Figure 12. The posterior-mean hotspot estimate is used for the reported thermal current calculation. Before bisection, the predicted hotspot temperatures at 400 and 1000 A are evaluated explicitly. Bisection is performed only when the 90 °C limit is bracketed within this validated domain. If the hotspot estimate at 1000 A remains below 90 °C, the result is reported as greater than 1000 A within the validated model domain, without extrapolation or a pseudo-root near the upper boundary. When bracketed, the midpoint current is evaluated iteratively and the last verified lower bound is retained when the current interval is no greater than 2.5 A or eight iterations have been completed. In the present simulation-based workflow, each candidate current is applied to the finite-element model to obtain the corresponding 11 surface temperatures, which are then supplied to the trained inversion model. The resulting current is a model-derived thermal limit, and the defective-state value is subsequently adjusted using Equation (35); the available ampacity margin M is determined as

$$M = I_{safe}^{\max} - I_{now} \tag{36}$$

where I_{now} denotes the operating current of the cable.

To verify the feasibility of the proposed method, three representative working scenarios are selected for assessment. The hotspot-temperature limit is fixed at 90 °C, and the defect-aware reduction coefficient is set to 0.9303. The corresponding assessment results are summarized in Table 9.

As shown in Table 9, the three cases represent different combinations of load current, ambient temperature, soil thermal conductivity, and defect conditions. Case 1 represents a healthy cable joint. With a load current of 600 A, the predicted hotspot temperature is 53.87 °C, which is well below the thermal limit. The corresponding maximum allowable current is estimated as 955.47 A, yielding an available ampacity margin of 355.47 A, indicating sufficient thermal capacity for further loading. Cases 2 and 3 correspond to defective cable joints, for which the heuristic derating coefficient is applied. In Case 2, the working current is 700 A, the ambient temperature is 28 °C, and the predicted hotspot temperature is 57.78 °C. After applying the proposed heuristic derating rule, the allowable ampacity decreases from 983.59 A to 915.03 A, reducing the available ampacity margin to 215.03 A. In Case 3, the ambient temperature is higher than that in Case 2, whereas the higher soil thermal conductivity improves heat dissipation and partially offsets the adverse effect of ambient temperature. Under the combined environmental conditions, the allowable ampacity is 921.58 A, which is slightly higher than 915.03 A in Case 2. Therefore, this difference results from the combined changes in ambient temperature and soil thermal conductivity rather than from soil thermal conductivity alone. These results indicate that defective cable joints may still satisfy the hotspot-temperature constraint while exhibiting a reduced ampacity margin, and that adverse thermal conditions, such as elevated ambient temperature and low soil thermal conductivity, further constrain the allowable current-carrying capacity. Therefore, hotspot temperature alone is insufficient for fully evaluating operational safety, whereas the proposed method provides a more comprehensive ampacity margin assessment by jointly considering hotspot temperature, defect state, and thermal operating conditions.

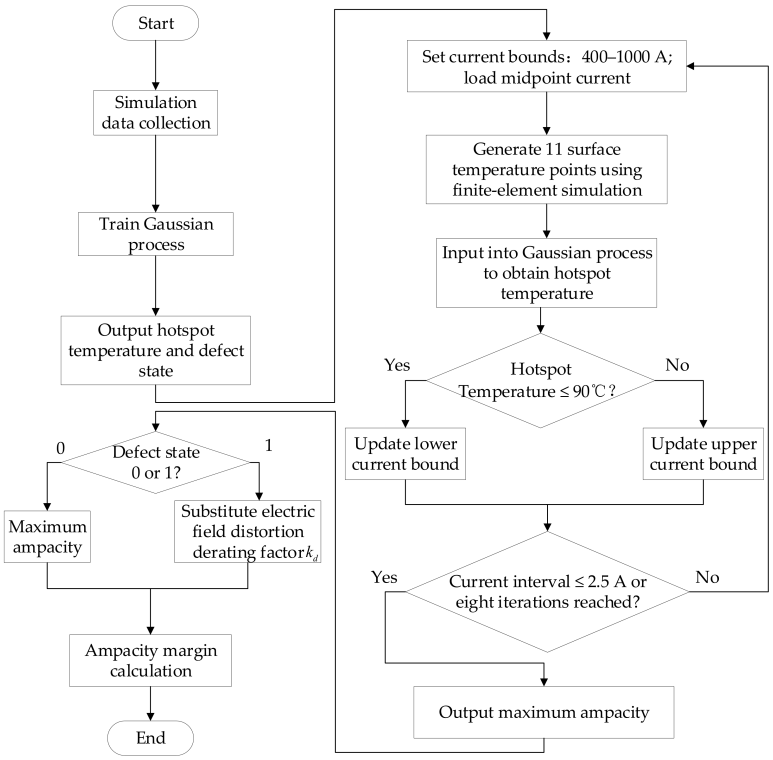

Figure 12. Flowchart of the simulation-based defect-aware ampacity margin assessment framework.

Table 9. Ampacity margin assessment results.

Case	Defect State	I_{now} (A)	T_{amb} (°C)	K_{soil} (W/(m·K))	T_p (°C)	θ	I^{max}_{search} (A)	I^{max}_{allow} (A)	M (A)
1	0	600	35	1.10	53.87	0	955.47	955.47	355.47
2	1	700	28	0.90	57.78	1	983.59	915.03	215.03
3	1	580	30	1.30	47.68	1	990.63	921.58	341.58

To check the thermal feasibility of the allowable-current estimates under the adopted assessment rule, the calculated currents are re-entered into the electro-thermal models under the three environmental cases. All hotspot temperatures remain below 90 °C. The maximum electric field along the selected radial path is also reported in Table 10.

Table 10 shows that the hotspot temperatures of all cases remain below the 90 °C thermal limit, indicating that the calculated currents satisfy the modeled thermal constraint under the adopted assessment rule. The radial electric-field values are reported as comparative indicators only, because no partial-discharge, breakdown, or insulation-lifetime threshold is incorporated into the present model. The equivalent water-tree model has the largest radial enhancement ratio of 2.116. Therefore, the back-substitution results verify only thermal compliance with the modeled 90 °C criterion and should not be interpreted as validation of dielectric safety.

To further illustrate the proposed method under different operating conditions, an illustrative daily load profile is constructed, as shown in Figure 13. Seven representative time points are selected from this profile, and each time point is treated as an independent steady-state condition using its corresponding load current, ambient temperature, soil thermal conductivity, and defect state. The condition at 18 h is classified as defective, while the remaining conditions are classified as healthy. The corresponding steady-state ampacity assessment results are presented in Table 11.

Table 10. Back-substitution thermal check of the baseline and defect-adjusted allowable-current estimates.

Condition	Allowable Current (Cases 1/2/3) (A)	Hotspot Temperature (°C)	Maximum Electric Field Along the Selected Radial Path (MV/m)
Defect-free	955.47/983.59/990.63	88.88–89.60	3.021
Air gap	888.87/915.03/921.58	80.73–82.03	2.988
Water film	888.87/915.03/921.58	80.45–81.81	3.072
Water tree	888.87/915.03/921.58	80.62–81.95	6.391
Metallic burr	888.87/915.03/921.58	80.70–82.01	3.046

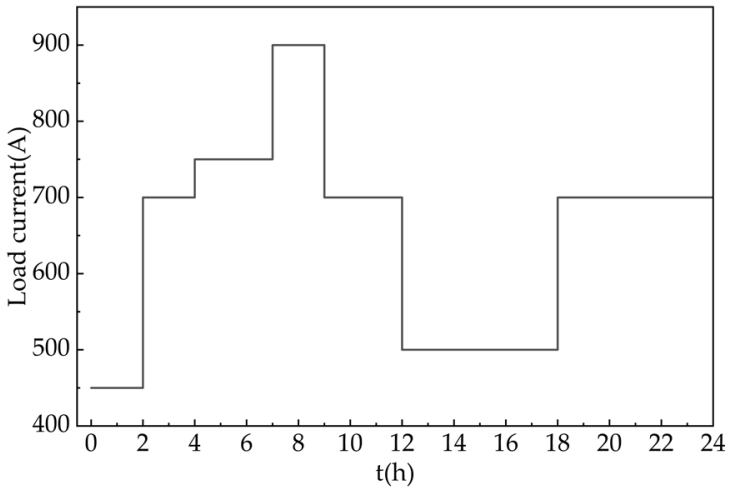

Figure 13. Illustrative daily load profile and selected representative steady-state evaluation points.

Table 11. Ampacity assessment results for seven representative steady-state operating points.

Time (h)	I (A)	T_{amb} (°C)	K_{soil} (W/(m·K))	θ	I_{allow}^{max}	M (A)
0	450	28.48	0.795	healthy	976.56	526.56
2	700	27.50	1.030	healthy	>1000	>300
4	750	29.00	0.980	healthy	990.63	240.63
7	900	27.32	1.034	healthy	>1000	>100
9	700	32.00	0.850	healthy	962.50	262.50
12	500	29.11	0.988	healthy	983.59	483.59
18	700	32.70	1.178	defective	901.95	201.95

Note: The reported current is the final assigned current after applying the state-dependent rule. For conditions classified as healthy, it equals the estimated thermal-limit current. For the condition classified as defective at 18 h, it includes the heuristic derating coefficient of 0.9303.

As shown in Table 11, the available current margin varies with the selected load and environmental conditions. Direct endpoint checks show that the 2 h and 7 h cases do not reach 90 °C at 1000 A; their thermal current limits are therefore reported as greater than 1000 A within the validated model domain, with margins greater than 300 and 100 A, respectively. No numerical root is assigned at or just below the upper boundary. At 18 h, the defective state invokes the illustrative derating rule, giving a heuristic-adjusted allowable current of 901.95 A and a margin of 201.95 A. These points are independent steady-state evaluations of representative segments of the illustrative load profile, not a continuous transient analysis.

Overall, the proposed defect-aware ampacity assessment framework integrates hotspot-temperature inversion, defect perception, and thermal operating conditions, enabling steady-state estimation of the remaining ampacity margin under specified operating conditions.

It provides a simulation-based methodological basis for further experimental and field validation of cable intermediate joints.

3.3. Validation of Model Generalization Ability

3.3.1. Validation Under New Operating Conditions for Represented Defect Configurations

To extend the geometric variability of the simulation dataset, 720 additional defective cases are generated. Four defect types, with three size levels (small, medium, and large) and three axial locations (−160, 0, and +160 mm), combine to give 36 defect configurations. For each of the 36 defect configurations, 20 operating conditions are sampled independently using Latin hypercube sampling over = 25 °C, I = 400–1000 A, T_{amb} = 10–40 °C, and k_{soil} = 0.5–2.5 W/(m·K). The random seed is determined by the configuration identifier to ensure reproducibility. Within each configuration, the 20 samples are sorted by current; odd-ranked samples are added to the original 1600 samples for training (1960 samples in total), while even-ranked samples form an independent 360-sample test set. This rule preserves balanced coverage of defect type, size, axial position, and current range. Because every tested configuration is represented in training and the subset contains no healthy cases, this split evaluates hotspot regression under new operating points for represented geometries; it is not treated as strict unseen-geometry or complete binary-classification validation. Figure 14 compares the predicted and simulated hotspot temperatures for the external test samples.

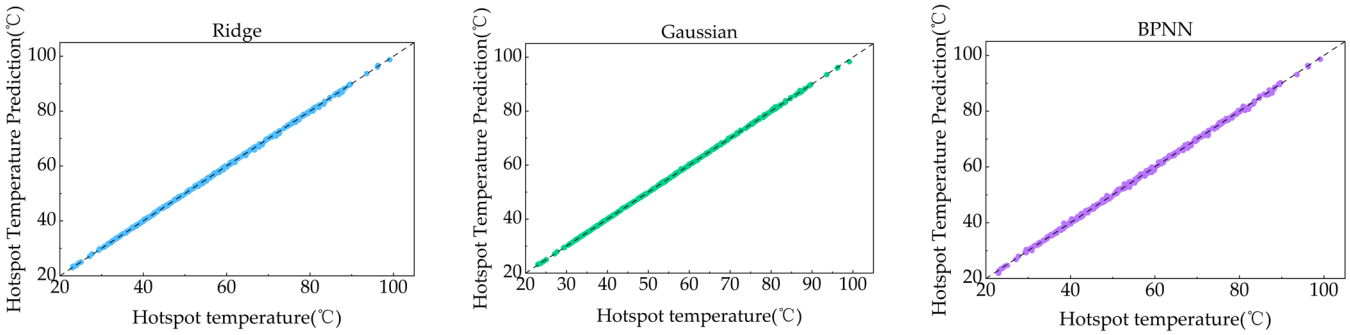

(**a**) Ridge (**b**) Gaussian (**c**) BPNN

Figure 14. Hotspot-temperature predictions for the independent 360-sample test set.

Figure 14 shows that the GPR model produces the most concentrated hotspot-temperature predictions around the ideal line. The corresponding regression metrics are summarized in Table 12, in which the 95th-percentile AE is the absolute hotspot-temperature prediction error below which 95% of the test samples fall. The GPR component's MAE, RMSE, and MaxAE are 0.1050, 0.1485, and 0.8452 °C, respectively, demonstrating good predictive performance under new operating conditions for defect configurations already represented in the training set. To further compare the error distribution and robustness of different inversion models, the absolute hotspot-temperature prediction errors on the external test set are presented in Figure 15. The GPR model also exhibits the narrowest hotspot-temperature error distribution and the lowest central error level, whereas the BPNN results are more dispersed. It should be noted that the external validation in this section is designed to evaluate model performance under new operating conditions within the represented defect-configuration space.

Table 12. Hotspot-temperature prediction performance on the independent 360-sample defective test set.

Model	MAE (°C)	RMSE (°C)	MaxAE (°C)	95th-Percentile AE (°C)
Ridge	0.1609	0.2361	0.9355	0.5947
Gaussian	0.1050	0.1485	0.8452	0.3132
BPNN	0.3031	0.4048	1.4633	0.8614

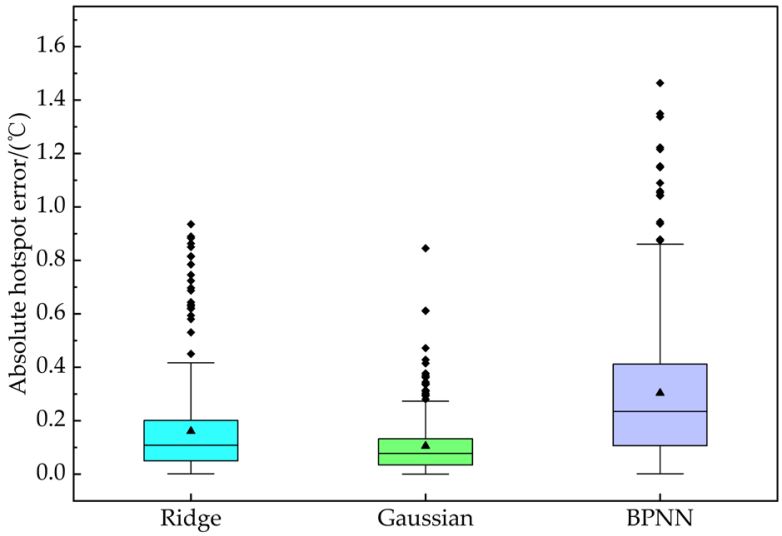

Figure 15. Absolute hotspot-temperature prediction errors for the independent 360-sample test set.

3.3.2. Complete Size- and Location-Holdout Validation

The complete defect-size and axial-location holdouts in this section provide the primary evidence of geometry generalization. To evaluate generalization to completely held-out defect sizes and axial locations without geometry overlap, each size level and axial location is excluded in turn from model training and used only for testing. The original dataset contains 800 defective samples, all corresponding to the medium-size, center-location reference configuration. Therefore, for the medium-size and center-location holdouts, these 800 original defective samples are also excluded from training. Together with the 240 matching defective samples from the expanded dataset, each of these holdouts contains 1040 defective test samples. After adding the same 160 independently held-out healthy samples, the total test-set size is 1200, leaving 1120 samples for training. For the small-, large-, left-, and right-holdout experiments, 240 matching defective samples from the expanded dataset are excluded from training and combined with the 160 held-out healthy samples, resulting in 400 test samples and 1920 training samples. In all holdout experiments, no defective sample sharing the held-out size or axial location remains in the corresponding training set. The results are shown in Table 13.

Table 13. Gaussian-model validation under strict defect-size or axial-location holdout.

Held-Out Geometry	N	MAE (°C)	RMSE (°C)	Accuracy	Recall	Specificity	FNR
Small size	400	0.0900	0.1236	0.9775	0.9750	0.9813	0.0250
Medium size	1200	0.1324	0.1693	0.7650	0.7288	1.0000	0.2712
Large size	400	0.1074	0.2699	0.9700	0.9667	0.9750	0.0333
Left location	400	0.0897	0.1274	0.9900	0.9958	0.9813	0.0042
Center location	1200	0.1407	0.1817	0.7767	0.7423	1.0000	0.2577
Right location	400	0.0871	0.1241	0.9400	0.9125	0.9813	0.0875

The strict geometry-level separation substantially changes the medium-size and center-location results because the 800 original fixed-geometry defective samples are no longer included in training. For the medium-size holdout, the Gaussian model achieves an MAE of 0.1324 °C, an accuracy of 0.7650, a recall of 0.7288, and an FNR of 0.2712. For the center-location holdout, the corresponding values are 0.1407 °C, 0.7767, 0.7423, and 0.2577, respectively. Across all six strict holdouts, the MAE ranges from 0.0871 to 0.1407 °C, the accuracy from 0.7650 to 0.9900, the specificity from 0.9750 to 1.0000, and the FNR from 0.0042 to 0.2712. These results indicate that classification performance decreases when representative geometrical conditions are completely absent from training. Because the medium-size and center-location holdouts also contain substantially fewer training samples than the other holdouts, their performance degradation reflects the combined effects of strict geometry exclusion and reduced training-data coverage. In a separate external test set containing 160 independently held-out healthy samples and 360 defective samples from represented defect configurations, the Gaussian model achieves an MAE of 0.0958 °C, an accuracy of 0.9712, a recall of 0.9694, a specificity of 0.9750, an FNR of 0.0306, and an AUC of 0.9956. This test evaluates performance under new operating conditions for represented defect configurations and therefore does not replace the stricter geometry-holdout evaluation.

3.3.3. Operating-Condition-Grouped Five-Fold Cross-Validation

As a supplementary evaluation of model repeatability across different data partitions, all 2320 samples are further evaluated using five-fold cross-validation grouped by the operating-condition triplet (I, T_{amb}, and k_{soil}). Samples belonging to the same operating group are assigned to the same fold. The 2320 samples form 2280 distinct operating-condition groups, with group sizes ranging from 1 to 2 and a mean group size of 1.018; 2240 groups (98.25%) contain only one sample. Therefore, exact-triplet grouping prevents identical operating conditions from appearing in both training and validation folds but provides only limited protection against broader data leakage. This evaluation is retained as a supplementary comparison of model performance and is not used as the primary evidence of geometry generalization or leakage prevention. The reported error bars represent the 95% confidence intervals of the five-fold-level results. Figure 16a compares the MAE of hotspot-temperature prediction for the ridge, Gaussian and BPNN models. The GPR model achieves the lowest hotspot-temperature MAE of approximately 0.0857 °C, followed by ridge at 0.1237 °C, whereas BPNN produces the largest error of 0.3332 °C. Meanwhile, the GPR component has a narrower 95% confidence interval, indicating relatively limited fold-to-fold variation under this supplementary evaluation. These results indicate that, under the present cross-validation setting, the GPR model best characterizes the nonlinear mapping between the input features and hotspot temperature for the research problem in this paper. Figure 16b shows the defect false-negative rate, defined as the proportion of samples with actual defects that are misjudged as normal. This indicator is vital for safety assessment, as false negatives may result in a failure to implement ampacity derating under defective conditions. The calibrated Gaussian-kernel ridge classifier has the lowest false-negative rate of 4.74%, compared with 7.65% for ridge and 8.03% for BPNN. Its narrow confidence interval indicates relatively limited fold-to-fold variation in the false-negative rate under this evaluation. The stricter assessment of generalization to geometrical conditions excluded from training is provided separately by the leave-one-size-out and leave-one-location-out evaluations in Section 3.3.2.

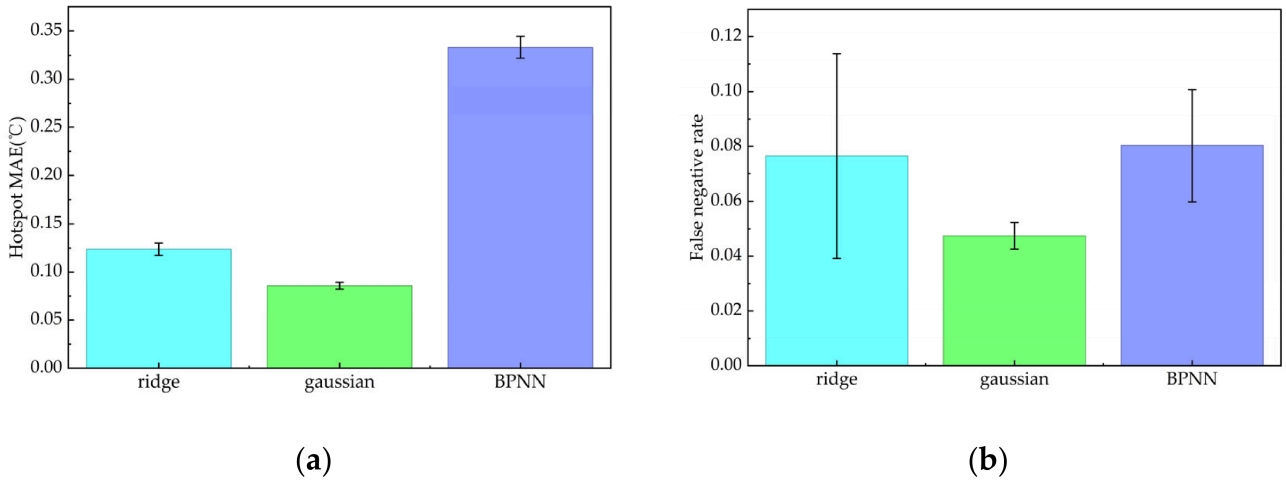

(**a**) (**b**)

Figure 16. Operating-condition-grouped five-fold cross-validation results: (**a**) hotspot-temperature MAE; (**b**) defect false-negative rate.

4. Conclusions

This paper proposes a simulation-based defect-aware ampacity margin assessment method for cable intermediate joints based on hotspot-temperature inversion. By integrating electro-thermal finite-element simulations with Gaussian-kernel inversion models, the proposed framework estimates hotspot temperature and identifies the binary insulation state under simulated operating conditions. Within the investigated model and parameter ranges, load current, ambient temperature, and soil thermal conductivity strongly influence hotspot temperature, whereas the soil-surface heat-transfer coefficient has a comparatively limited effect for the present buried configuration. The modeled insulation defects produce only small changes in surface temperature but cause pronounced local electric-field redistribution. The electric-field results are used to characterize the relative severity of the modeled defect conditions rather than to establish a validated dielectric safety threshold. Under noise-free simulation conditions, the Gaussian-kernel framework achieves a hotspot-temperature MAE of 0.075 °C and demonstrates the numerical separability of healthy and defective insulation states within the simulated dataset. Validation under new operating conditions for represented defect configurations shows good hotspot-temperature prediction performance, while the strict size- and location-holdout tests show that classification performance decreases when representative geometrical conditions are completely absent from training. The operating-condition-grouped five-fold cross-validation is retained only as a supplementary model-comparison and repeatability evaluation. Therefore, the generalization evidence is limited to the investigated simulated defect-size and axial-location ranges.

A defect-aware ampacity assessment framework is further established by combining bisection-based thermal-limit current calculation with a heuristic defect derating coefficient. The resulting defect-adjusted allowable currents reflect the adopted derating rule rather than an independently predicted thermal consequence of the insulation defects. Back-substitution for the three nominal scenarios examined confirms that these currents satisfy the modeled 90 °C thermal constraint under the corresponding simulated conditions. However, these limited verification cases do not fully establish the accuracy of the predicted current limits across different operating conditions, particularly regarding potential hotspot-temperature underestimation near the 90 °C limit. Therefore, the reported current values are model-specific estimates under the adopted geometry, material properties, contact-resistance setting, loss formulation, environmental boundary conditions, and heuristic derating rule. Furthermore, measurement noise may lead to missed defects and prevent the activation

of the heuristic derating rule, limiting its reliability under practical monitoring conditions. For practical applications, the simulation dataset should cover a comprehensive range of potential defect types, sizes, and locations to improve the representativeness of the training data and the model's adaptability to actual operating conditions. Since the present study is based on numerical simulations, future work includes laboratory measurements, analysis of signed prediction errors near the thermal limit, and validation against additional independent FEM cases to further assess the accuracy and practical applicability of the proposed framework.

Author Contributions: Conceptualization, X.W. and G.Z.; methodology, P.L. (Pei Li), Y.L. and G.Z.; software, P.L. (Pei Li) and X.W.; validation, M.C. and X.W.; formal analysis, B.Z. and P.L. (Peng Lin); investigation, X.W. and P.L. (Peng Lin); resources, M.C.; data curation, P.L. (Peng Lin); writing—original draft preparation, M.C. and P.L. (Pei Li); writing—review and editing, X.W., Y.L. and G.Z.; visualization, P.L. (Pei Li); supervision, Y.L. and G.Z.; project administration, M.C., X.W., B.Z. and P.L. (Peng Lin); funding acquisition, M.C., X.W., B.Z., P.L. (Peng Lin) and G.Z. All authors have read and agreed to the published version of the manuscript.

Funding: This research is funded by the National Natural Science Foundation of China under Grant No. 52377017 and the Self-funded Research Project of Taizhou Hongchuang Electric Power Group Co., Ltd. Grant No. 521184250003.

Data Availability Statement: Data will be made available on request.

Conflicts of Interest: Author Mingxu Chen, Xueyan Wang, Bingye Zhang, Peng Lin were employed by the company Taizhou Hongchuang Electric Power Group Co., Ltd. The remaining authors declare that the research was conducted in the absence of any commercial or financial relationships that could be construed as a potential conflict of interest.

References

1. International Electrotechnical Commission. *Electric Cables—Calculation of the Current Rating—Part 1-1: Current Rating Equations (100% Load Factor) and Calculation of Losses*; General; IEC 60287-1-1 Edition 1.2-2001; International Electrotechnical Commission: Geneva, Switzerland, 2001.
2. International Electrotechnical Commission. *Calculation of the Cyclic and Emergency Current Rating of Cables—Part 2: Cyclic Rating of Cables Greater than 18/30 (36) kV and Emergency Ratings for Cables of All Voltages*; IEC 60853-2 AMD 1-2008; International Electrotechnical Commission: Geneva, Switzerland, 2008.
3. Li, H.; Zhang, Y.W.; Zhang, R.X. Simulation of temperature field and current carrying capacity of direct buried XLPE cables under different laying conditions. *Electr. Power Eng. Technol.* **2023**, *42*, 169–177.
4. Liu, W.B.; Xie, M.J.; Zhou, Y.; Ma, G.Q.; Hang, M.M.; Zhang, H. Effects of Microstructural Parameters of Soil on Temperature and Ampacity of the Buried Cables. *High Volt. Eng.* **2024**, *50*, 749–757. [CrossRef]
5. LI, Q.S. Study on Evolution and Optical Fiber Temperature Inversion Method for Submarine Cable Burial Depth. Master's Thesis, South China University of Technology, Guangzhou, China, 2024.
6. Zhang, Y.T.; Yu, F.H.; Ma, Z.; Li, J.; Qian, J.; Liang, X.J.; Zhang, J.Z.; Zhang, M.J. Conductor Temperature Monitoring of High-Voltage Cables Based on Electromagnetic-Thermal Coupling Temperature Analysis. *Energies* **2022**, *15*, 525. [CrossRef]
7. Wu, T.; Zhu, H.S.; Zhan, Q.H.; Wang, N.J. A Precise Inversion Method of Cable Joint Core Temperature with Non-Embedded Detection Based on UMAP and ISSA-BPNN. *Front. Energy Res.* **2022**, *10*, 1028423. [CrossRef]
8. Zhang, Z.; Liu, W.; Zeng, L.; He, S.; Zhou, H.; Ruan, J. Long-Term Ampacity Prediction Method for Cable Intermediate Joints Based on the Prophet Model. *Processes* **2024**, *12*, 748. [CrossRef]
9. Zhang, Z.L.; Zhao, H.; Yang, Y.; Liu, X.L.; Xiao, J.Y. Temperature Analysis and Ampacity Evaluation of HV Cable Joints Based on Thermal Flow Coupling and Measurable Data. *Sci. Rep.* **2025**, *15*, 27942. [CrossRef]
10. Liang, G.J.; Wang, Z.G.; Lin, W.H.; Deng, Y.Q.; Xiao, C. Study on temperature inversion monitoring of 110 kV single core cable intermediate joint. *Distrib. Util.* **2023**, *40*, 62–71. [CrossRef]
11. Song, Y.L.; Wu, T.; He, Q.; Zhu, H.S. Hot Spot Temperature Inversion Method of Locally Sheathed Cable Based on LassoNet-ISSA-BP Neural Network. *South. Power Syst. Technol.* **2025**, *19*, 158–167.
12. Wu, T.; Zhu, H.Q.; Zhan, Q.H. Indirect Measurement Method of Cable Joint Core Temperature Based on BP Neural Network Optimized by Improved SSA. *Sci. Technol. Eng.* **2023**, *23*, 9048–9055.

13. Gao, W.C.; Chang, J.; Hang, B. Design of Intelligent Temperature Monitoring System for Cable Joints Based on Deep Neural Networks. *Technol. Mark.* **2025**, *32*, 86–89.
14. Pang, K.; Feng, L.; Deng, W.C. Inversion of cable internal temperature based on microwave radiation measurement and GA-BP neural network. *J. Henan Polytech. Univ. (Nat. Sci.)* **2024**, *43*, 146–153. [CrossRef]
15. Li, G.Y.; Yan, S.Y.; Wang, X.Y.; Wang, H.L.; Liu, S.Z. Study of Temperature Distribution in Cable Defects Based on COMSOL. *Mech. Electr. Technol.* **2026**, *50*, 57–61+97. [CrossRef]
16. Lu, X.; Hu, R.; Lan, R.; Tian, J.; Wei, Y.; Li, G. Effect of Interface Defects on the Electric–Thermal–Stress Coupling Field Distribution of Cable Accessory Insulation. *Energies* **2024**, *17*, 4498. [CrossRef]
17. Yang, B. Impact Analysis and Identification of Typical Defects in Intermediate Joints of 10 kV XLPE Cables. Master's Thesis, Shenyang Agricultural University, Shenyang, China, 2025.
18. Li, H.M. Modeling and Analysis of Electric Field Distribution for Small Defects in 10 kV Cable Joints. Master's Thesis, North China Electric Power University, Beijing, China, 2021.
19. Deng, J.Y.; Wang, X.H.; Nie, Y.X. Simulation Research on Electric Field Distribution of 10 kV XLPE Cable Intermediate Joint Defect. *Wire Cable* **2023**, *66*, 47–53. [CrossRef]
20. Huang, B.; Yang, M.Y.; Nie, Y.J.; Zhao, X.T.; Xu, X.S.; Li, H.W. Effect of various impurity defects on electrical performance of cable intermediate joints. *Adv. Technol. Electr. Eng. Energy* **2025**, *44*, 42–54.
21. Zhou, Y.Y.; Zhang, Z.S.; Zhang, L.X.; Yao, S.J. Effects of Defects on Electric Field Distribution and Regional Temperature of Cable Joints under Electromagnetic-thermal Coupling. *Proc. CSU-EPSA* **2025**, *37*, 66–74. [CrossRef]
22. He, J.H.; He, K.; Dong, B.W. Electric field characteristics investigation and electrical tree propagation of distributed network cable joint with defects. *Electr. Power Eng. Technol.* **2023**, *42*, 154–161.
23. Wu, W.; Wang, F.; Huang, Z.W.; Wang, Y.Q. Simulation analysis of electric-thermo field of 110 kV power cable joint. *Transducer Microsyst. Technol.* **2011**, *30*, 15–17, 21. [CrossRef]
24. Nie, Y.; Luo, R.C.; Wang, W.; Hua, Y.Y. Analysis of Electric Field Distortion Characteristics at Defects of 220 kV XLPE Cable Joints. *J. Electr. Power* **2024**, *39*, 377–388. [CrossRef]
25. Wei, Z.P.; Xu, R.R.; Zhang, H.; Liu, S.Y.; Lin, G.Z. Effects of Different Defects on Electric-thermal Field Distribution Characteristics of 220 kV Cable Joints. *Proc. CSU-EPSA* **2025**, *37*, 126–132. [CrossRef]
26. Lu, H.R. Simulation Analysis of Crimping Defects and Temperature Distribution of Multi-physics Coupling Single-core Cable Joint. *Electr. Eng.* **2024**, *45*, 105–108. [CrossRef]
27. Tian, Y. Study on Electric Field Distribution of High Voltage Cable Joint Under Transient Shock. Master's Thesis, Xi'an University of Technology, Xi'an, China, 2024.
28. Wang, F.J.; Yao, T.Y.; Yang, Z.R.; Wang, D.H.; Dong, X.J. Magnetic Field Distribution Characteristics of 110 kV XLPE Cable Joint and Its Degradation Evaluation. *Proc. CSU-EPSA* **2022**, *34*, 51–53. [CrossRef]
29. Ju, C. Electric field simulation of temperature measuring device at middle junction of high voltage cable. *Autom. Instrum.* **2023**, *43*, 338–342. [CrossRef]
30. Tariq, R.; Alhamrouni, I.; Rehman, A.U.; Tag Eldin, E.; Shafiq, M.; Ghamry, N.A.; Hamam, H. An Optimized Solution for Fault Detection and Location in Underground Cables Based on Traveling Waves. *Energies* **2022**, *15*, 6468. [CrossRef]
31. Li, K. Small Sample Image Recognition Based on Gaussian Process Classification. Master's Thesis, Qingdao University, Qingdao, China, 2024.
32. Guan, D.Y.; Wang, H.Y.; Wang, K. Study on Adaptive Signal Control for Dynamic Throughput Capacity Based on Gaussian Process Regression. *J. Transp. Syst. Eng. Inf. Technol.* **2026**, *26*, 137–147. [CrossRef]
33. Wang, C.; Hui, Z.; Shi, Z.; Liao, H.; Hou, Q.; Sun, Y. Early Predicting State of Health of Lithium-Ion Battery Based on Dynamic Dataset Partitioning and Optimized Gaussian Process Regression. *J. Energy Storage* **2026**, *174*, 123209. [CrossRef]
34. Liu, C.; Ruan, J.J.; Huang, D.C.; Zhan, Q.H.; Xiao, W.; Tang, K. Hot spot temperature of cable joint considering contact resistance. *High Volt. Eng.* **2016**, *42*, 3634–3640. [CrossRef]
35. Zeng, L.C.; Meng, C.X.; Luo, H.X.; Wang, W.P.; Hou, A.G.; Chan, Q.Z. An inverse model for axial temperature in three-core cable joints and sensitivity analysis of material parameters. *Zhejiang Electr. Power* **2024**, *43*, 94–103.
36. Liu, G.; Wang, Z.H.; Xu, T.; Liu, Y.G.; Wang, P.Y. Current capacity calculation and experimental analysis of 110 kV cable joint. *High Volt. Eng.* **2017**, *43*, 1671–1676. [CrossRef]
37. Zhao, X.F.; Hao, Y.F.; Huang, G.Q.; Duan, W.; Sun, H.F.; LI, J.M.; Chen, X.; Deng, J.B. Calculation on Steady-state Current Carrying Capacity of Intermediate Joint of Direct Buried Cable Based on the Finite Element Simulation. *High Volt. Appar.* **2022**, *58*, 64–70, 85. [CrossRef]
38. Boggs, S.; Densley, J.; Kuang, J. Mechanism for Impulse Conversion of Water Trees to Electrical Trees in XLPE. *IEEE Trans. Power Del.* **1998**, *13*, 311–315. [CrossRef]

39. Acedo, M.; Frutos, F.; Torres, M.; Filippini, J.C. The Cylindrical Capacitive Model for Water Treeing Degradation in Extruded HV Cables. In Proceedings of the 1995 IEEE 5th International Conference on Conduction and Breakdown in Solid Dielectrics, Leicester, UK, 10–13 July 1995; pp. 661–665.
40. Boonraksa, T.; Promvichai, N.; Supanarapan, T.; Minja, K.M.; Chombo, P.V.; Marungsri, B. Simulation of Electric Field Distribution in Water Treed XLPE HV Underground Cable Using COMSOL Multiphysics. In Proceedings of the 5th IIAE International Conference on Industrial Application Engineering, Kitakyushu, Japan, 27–31 March 2017; pp. 267–270.

Disclaimer/Publisher's Note: The statements, opinions and data contained in all publications are solely those of the individual author(s) and contributor(s) and not of MDPI and/or the editor(s). MDPI and/or the editor(s) disclaim responsibility for any injury to people or property resulting from any ideas, methods, instructions or products referred to in the content.